Local Ultrasonic Resonance Spectroscopy of Lithium Metal Batteries for Aerospace

Applications

A Thesis presented to the Graduate Faculty of the

Department of Electrical and Computer Engineering

University of Virginia

in partial fulfillment for the degree

Master of Science

By: William Charles Nelson

December 2021

Committee

This thesis is submitted in partial fulfillment of the requirements for the degree of

Master of Science

Author: William Nelson

This Thesis has been read and approved by the examining committee:

Advisor: Dr. Mool Gupta

Committee Chair: Dr. Zongli Lin

Committee Member: Dr. Gary Koenig

Committee Member: Dr. Erik Frankforter

Accepted for the School of Engineering and Applied Science:

Jennifer L. West, School of Engineering and Applied Science

December 2021

Acknowledgments

Firstly, I would like to thank my advisor, Dr. Mool Gupta, for all of his guidance and for allowing me this opportunity to work with the National Institute of Aerospace (NIA) and at NASA Langley Research Center (LaRC) where this work was performed.

I would like to extend my deepest thanks to Erik Frankforter for serving as a technical advisor for my work and for his constant support. With his direct guidance on my work and our weekly one-on-one meetings, almost everything that I have learned and accomplished over these past two years has been a great part, thanks to Erik. I would also like to thank Daniel Perey for allowing me on the Sensors-based Prognostics to Avoid Runaway Reactions and Catastrophic Ignitions (SPARRCI) team and for his constant advice and support throughout my time at LaRC. Also, Pat Johnston has been essential for providing feedback on my work with his vast expertise. Many thanks to Peter Juarez for training me on the lab equipment I needed to perform my work as well.

In addition, I would like to thank the rest of the members of the NASA LaRC Nondestructive Evaluation Sciences Branch (NESB). While the mandatory teleworking made interacting with everybody a little unusual, I really enjoyed their joyous attitude and kindness every day. I would also like to extend my thanks to the rest of the SPARRCI team with whom I performed this work.

Abstract

As next-generation aircraft and vehicles continue to develop, so do their associated energy demands. Lithium metal batteries are a leading candidate to fulfill this energy requirement, but these batteries are prone to internal dendrite defects that can lead to catastrophic thermal runaway events. Current battery management systems are capable of mitigating such risks, but are unable to detect such defects until thermal runaway has already begun. Various nondestructive evaluation (NDE) techniques, particularly ultrasonic NDE, can directly monitor internal battery parameters giving them the potential to detect critical defects prior to catastrophic failure. However, most of the current battery NDE research has focused on improved battery state-of-charge (SOC) and state-of-health (SOH) monitoring with little emphasis on critical defect detection. Thus, a measurement technique sensitive to subtle battery defects is needed. In addition, the complex mechanics of ultrasound in porous, thin, multilayered batteries prompt the use of physics-based simulation to guide inspections.

In this work, an ultrasonic NDE technique has been developed utilizing frequency domain analysis of local battery resonances to detect the presence of battery defects. This technique is a practical extension of local ultrasonic resonance spectroscopy (LURS) – which previously required non-contact laser ultrasonics – to measurements with piezoelectric contact and immersion scan transducers. To extend the technique to work with piezoelectric transducers, ultrasonic battery measurements were compared to a sans-battery calibration measurement. Then, a linear systems deconvolution was used to eliminate the transfer functions of extraneous factors such as the transducer and electronics, leaving only the frequency-dependent battery reflection coefficient.

The LURS technique was first validated on stainless steel and aluminum plates, producing reflection coefficients in line with analytical and numerical finite element modeling (FEM) results.

Functioning Li-metal pouch cells were then seeded with lithium chip defects prior to LURS measurements. The presence of these defects is shown to cause a measurable shift in the battery's through-thickness local resonances. 2D, frequency-domain poroelastic models of ultrasonic propagation in a single-cell lithium metal pouch battery were created and corroborated these findings. Thus, this work has both extended and proven the feasibility of the LURS technique in the detection of local battery defects.

Table of Contents

Chapter 1: - Background and Motivation

With the constantly evolving landscape of electric vehicles and devices, there has been a parallel growth in demand for an efficient, lightweight energy storage solution for these systems. This has brought great interest to lithium metal batteries for their high energy densities and reusability [1]. However, lithium metal batteries are prone to failure and have limited lifetimes due to various aging phenomena [2]. Thus, these batteries need to be constantly monitored to ensure safe and efficient operation. Conventional battery management systems, however, are unable to detect certain catastrophic defects that greatly increase the associated safety risks in using lithium metal batteries.

In particular, these batteries are prone to defects in which lithium dendrites grow across the battery from one electrode to the other, causing an internal short circuit. This ultimately leads to a thermal runaway reaction in which the heating and ignition of one battery cell can cascade into the ignition of neighboring cells. In recent years, a large percentage of fires in electric vehicles has been due to this thermal runaway effect in lithium batteries [3]. The current solution to this has been to engineer around such reactions and place the batteries in bulky containment systems to isolate them from other cells [4]. This only passively prevents thermal runaway from occurring and adds significant weight to the batteries, which is very undesirable in aerospace applications. This issue has caused a large amount of research to go into minimizing parasitic mass and volume in battery component designs [5].

Nondestructive evaluation (NDE) techniques have the potential to detect precursors and development of critical defects prior to the occurrence of a catastrophic failure due to their ability to probe internal features of materials. For battery health monitoring, these techniques would need to be field-deployable and the physical mechanisms of the inspection would need to be understood

well to provide confidence in the inspection technique. This work seeks to accomplish this through physics-based modeling and the development of an ultrasonic frequency domain technique sensitive to embedded battery defects. In the next sections, the basic working principles and critical defects of lithium metal batteries are discussed, in addition to current battery health monitoring techniques.

1.1 **Lithium Metal Batteries**

Li-metal batteries are complex, multilayered structures comprised of solid, liquid, and porous layers. The fundamental unit cell of a Li-metal battery is composed of two active electrodes, each with an attached current collector. The battery chemistry of interest in this work is comprised of a solid lithium anode with a copper current collector and a porous $LiCoO_2$ cathode with an aluminum current collector. Figure 1 shows the unit cell of such a single cell battery. A porous separator material is placed between the anode and cathode to prevent internal short circuits, and it is filled with a liquid electrolyte which allows ions to transfer between the electrodes. In practice, there are multiple cells comprised of this single-cell structure stacked many times [6].
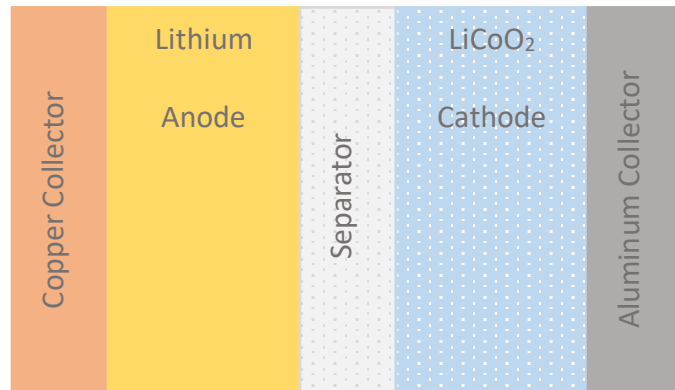

Figure 1: Layout of a single cell lithium metal battery

In operation, lithium ions exchange between the two electrodes, depositing onto the surface of the lithium anode during charging and intercalating into the pores of the $LiCoO_2$ cathode during

discharging. This results in various mechanical property changes in density, modulus, and porosity [7].

During the fabrication of the battery, the electrolyte and lithium anode oxidizes, forming a thin layer known as the solid electrolyte interface (SEI). In this layer, lithium plating can occur in which lithium ions are reduced to metallic lithium and build up at the interface. This lithium is no longer usable in standard battery operation and will thus result in an overall loss of charge capacity. This is a normal aging phenomenon in lithium-based batteries and is generally why these types of batteries have a limited lifetime. However, under various cycling conditions, such as low temperature or high charge/discharge rates, this plating can occur non-uniformly and form needle-like structures known as dendrites. Dendrites can penetrate the battery separator, short circuit the electrodes, and cause a thermal runaway reaction to occur [8]. This process is further emphasized in Figure 2.
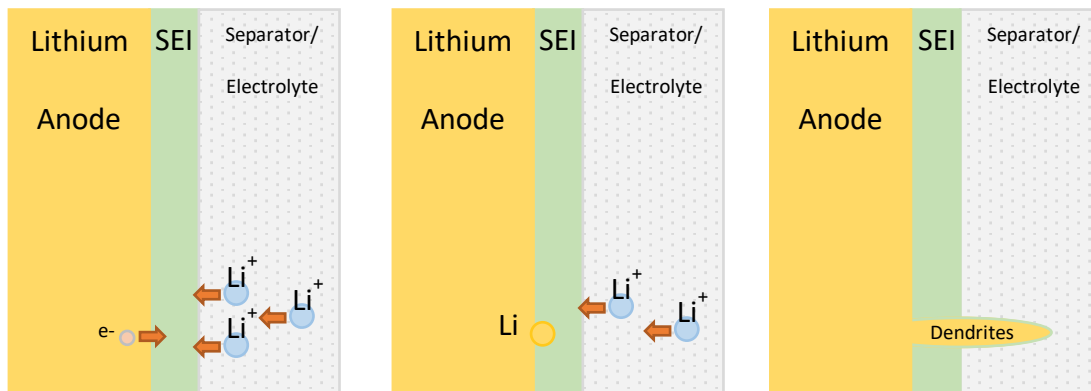
Figure 2: Conceptual sketch of how lithium plating can lead to dendrite growth

Dendrites have received lots of attention due to their common occurrence, their potential for catastrophic failure, and their difficulty of detection. However, there are other important battery defects that can occur [2]. Gas generation from the decomposition of the electrolyte solvent can

lead to increased cell temperatures and thus thermal runaway. Continued reduction of lithium ions can cause further thickening of the SEI layer and an overall loss in charge capacity and performance of the battery. From an ultrasonic NDE perspective, there are local changes in geometry and material properties associated with each of these defect mechanisms and thus the potential for detection based on the amount of influence they have on wave propagation and wave-defect interaction within the battery.

1.2 Current Battery Monitoring Techniques

1.2.1 Battery Management Systems

As mentioned before, the current solution to prevent dendrites from causing thermal runaway is to engineer safe containment systems and constantly monitor the batteries. These tasks are accomplished with a battery management system (BMS) which is used to ensure maximum operating efficiency and mitigate battery failure. The most basic way in which a BMS does this is through the state of charge (SOC) and state of health (SOH) monitoring. The SOC of a battery is the ratio of the battery's current charge to its maximum capacity and is the most important of these parameters as it is essentially the 'fuel gauge' that can determine how much energy is left in the battery. The battery's SOH is representative of the battery's deterioration from aging and is usually tracked by monitoring changes in maximum SOC over time.

There are various different SOC and SOH estimation algorithms and models, but they mostly all involve using external cell parameters such as voltage, current, and temperature as inputs for lookup tables and computational models that then predict the overall SOC [9]. As these methods all lack information about internal battery changes, there is a degree of inaccuracy to their predictions that can accumulate in error over time. For this same reason, these methods are not

sensitive to the development of some critical battery defects [2]. Ultrasonic nondestructive evaluation (NDE) techniques, however, have the advantage of directly monitoring internal battery changes, thus making them effective at SOC/SOH monitoring and also sensitive to defects, and is why they have been of great interest recently [7].

1.2.2 Battery NDE Review

NDE techniques have become a large research area for battery health monitoring due to their ability to probe the internal mechanics of a battery with little interference. This allows the acquisition of internal battery information that modern BMS's cannot normally acquire. Nuclear magnetic resonance spectroscopy has been shown capable of detecting lithium dendrite growth and various battery aging/degradation phenomena during in-situ battery operation [10-11]. These techniques have given great insight into these phenomena; however, they suffer from requiring extensive lab equipment, making them undesirable for a real battery application. Thermography techniques have been used to detect gas pocket defects and analyze the thermal behavior of batteries under abuse scenarios [12-13]. Thermography techniques have not been shown capable of obtaining any information about battery SOC independently, however. While these various NDE techniques have proven applicable for battery inspections in some form, the vast majority of research thus far has focused on ultrasonic techniques due to their promise for a field-deployable inspection technique capable of improved SOC/SOH and defect monitoring [7].

Much of this ultrasonic NDE work has been in the realm of SOC and SOH determination. The feasibility of these techniques was initially demonstrated in a study by Hsieh et al., which showcased how the relationships between battery SOC and mechanical properties can be used to accurately predict SOC via acoustic measurements and modeling [14].

Since then, this area has been expanded on greatly, with various other applicable techniques being developed [7]. Ladpli et al. have demonstrated methods of using ultrasonic guided waves to reliably track a battery's SOC and SOH [15]–[18]. The time of flight and signal amplitude of pitch-catch guided waves were shown to have direct correlations to the battery's SOC due to the changes in modulus and density associated with the charging and discharging process. An analytical model of this process was constructed and was able to reliably validate the experimental results.

Gold et al., related ultrasonic measurements to poroelastic properties of internal battery components [19]. Because of the intercalation of ions into the porous electrodes, there are porosity changes associated with changing battery SOC. This relationship was mapped using Biot poroelastic waves theory and through-transmission ultrasonic inspections.

At the time of writing this, the majority of current research has been focusing on determining battery SOC via ultrasound, with only a few studies done on using these techniques to directly detect battery defects or failure conditions. Bommier et al. used through-transmission ultrasound to relate changes in time of flight to lithium plating from uneven charge rates [20]. The extent of lithium plating was then confirmed by postmortem electrochemical analysis of the battery electrodes. Another study was done by Robinson et al. in which portions of a battery's electrodes were removed, which was detectable via ultrasonic inspection [21]. These studies show promising results in using ultrasound to detect coarse battery defects, however, their time-domain analysis methods are not generally suitable for handling idiosyncrasies of layered media, so further technique development and analysis is required to demonstrate that ultrasonic NDE is generally suitable for battery defect detection.

In addition, there has also been very little work on ultrasound battery simulations, especially with battery defect conditions. In the works discussed previously by Ladpli et al. and for SOC/SOH estimation, analytical models were built from 1D elastic wave assumptions that were capable of accurately describing acoustic velocity changes associated with charging/discharging [15 – 18]. Gold et al. did a similar study except included poroelastic theory to better represent the physics of the electrolyte-filled porous cathode [19]. One recent study by Li and Zhou simulated an air-coupled ultrasonic inspection of an entire battery system with embedded stomata defects at various layers [22]. These defects were able to be detected through analyzing the attenuation of signal amplitude in both the time and frequency domains. These studies have laid the groundwork for ultrasound battery simulation and determined important considerations for accurate representation of the internal physics of a battery. However, there are still gaps in modeling defect conditions, especially with those seen in typical battery operation.

To expand on these studies, this thesis seeks to investigate the feasibility of a normal incidence frequency domain ultrasound inspection technique in the detection of internal battery defects. A contact technique was chosen due to the simple setup and ease in which a field-deployable technique could be realized from it, with further possibility for direct extension via embedded sensors on the surface or inside the battery. The complex, layered media was handled by frequency-domain post-processing and deconvolution to isolate the battery's local through-thickness spectral response. In the next sections, a simple single-layer case will be investigated to establish the technique, and then it will be applied to a full battery inspection.

Chapter 2: Local Ultrasound Resonance Spectroscopy Technique

2.1 **Measurement and Modeling Approach**

In a pulse-echo ultrasound inspection setup, an incident ultrasound wave excited from a transducer propagates through the specimen being inspected. These waves reflect off the specimen's internal features and interfaces, propagate back through the specimen, and then are picked up by the same excitation transducer. In sufficiently thick specimens, these reflections show up as distinct waveforms in the received time-domain signal. Then, by looking at the time that these signals are received, the corresponding location/thickness of features in the specimen can be determined by using the material's wave speed. This is known as the time of flight and is a key parameter for ultrasound inspections [23]. If the specimen being inspected has very thin layers, as with a lithium metal battery, the time of flight will be very short, and reflections will overlap with the original signal in time. This makes time-domain analysis very difficult as there will be no distinct reflections in the signal to measure. In some cases, this might be mitigated by inspecting at high frequencies, but this still leaves significant challenges in interpreting waveforms with many transmissions/reflections between layered battery materials. In these cases, a different approach must be taken to reliably extract information about the specimen.

The most common method to resolve this issue is to look at the frequency domain information of the reflected waveforms. This is common in applications in which measuring the thickness of a thin adhesive or lubricant layer is desired [24], [25]. At the through-thickness resonances of this layer, the incident wave predominantly transmits through the specimen, and the frequency-dependent reflection coefficient reaches a minimum value. The resonance frequency in which this phenomenon occurs is then used to calculate the thickness and material property information of the specimen. If measuring below the first through-thickness resonance, the

reflections will be dominated by the stiffness of the specimen, and thus a mass-spring model can be used to calculate the material properties [24].

Resonant Ultrasound Spectroscopy (RUS) is another frequency domain NDE technique that measures the free mechanical vibrations of an entire specimen [26]. As with the previous technique, resonant frequencies are measured and used to gain information about the specimen's mechanical properties. Local Ultrasonic Resonance Spectroscopy (LURS) is a very similar technique except that it focuses on measuring resonances in localized regions of the specimen rather than across the entire specimen [27]. Defects that are present in those regions create different resonance behaviors than in pristine regions, which can then be used as a method of defect detection. The LURS technique requires a broadband frequency range and so far has required a non-contact method such as laser or air-coupled ultrasound to get the free, mechanical resonances of the system.

In this work, the reflection coefficient measurement approach is used to extend the LURS technique to be applicable for contact transducers. This gives a localized, frequency-dependent reflection signal that contains information about local mechanical resonances in a lithium metal battery. Since these resonances depend on local material properties and thicknesses, this reflection signal can be used to detect the presence of defects. To do this, a linear systems deconvolution approach is applied to the measurement system to isolate the battery's mechanical resonances and makes this method applicable for use with a contact setup. This is described in more detail in Section 2.4.2. To better understand how this technique will work, a simple model of a single layer inspection is built in the next section and will serve as a lens for validating and interpreting this contact transducer extension of the LURS technique.

2.2 **Analytical Modeling**

A 1D model layout of a pulse-echo inspection on a single layer material submerged in water is shown below in Figure 3. Assuming infinite surrounding water domains, the system can be explained by looking at the incident, reflected, and transmitted pressure waves. This is a derivation of a classical acoustics problem and follows the analysis used by Kinsler et al. [28], but is presented here for the necessary context of this work. The equations for the incident, reflected, and transmitted pressure waves can be seen in Equations (2.1 - 2.5). Because of the infinite water boundaries, there is no reflected wave from the second water domain back into the system. This also means that the pressure waves are in the far-field away from any interfaces where evanescent wave modes may interfere.
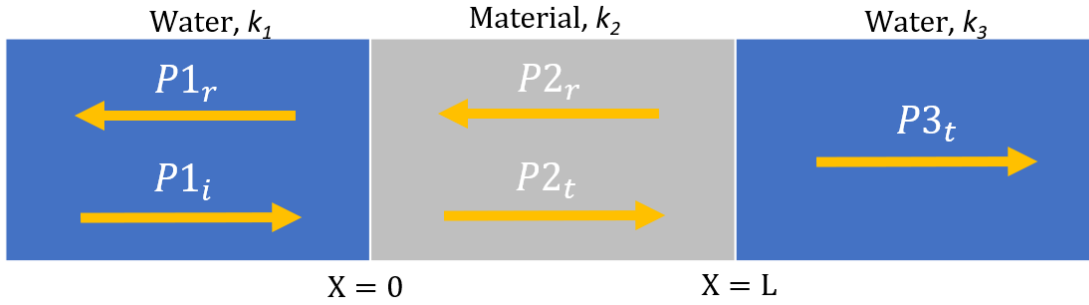

Figure 3 Diagram showing the layout of the 1D analytical model

$$P1_i(x, t; \omega) = \widehat{P1}_i e^{i(\omega t - k_1 x)} \qquad (2.1)$$

$$P1_r(x, t; \omega) = \widehat{P1}_r e^{i(\omega t + k_1 x)} \qquad (2.2)$$

$$P2_t(x, t; \omega) = \widehat{P2}_t e^{i(\omega t - k_2 x)} \qquad (2.3)$$

$$P2_r(x, t; \omega) = \widehat{P2}_r e^{i(\omega t + k_2 x)} \qquad (2.4)$$

$$P3_t(x, t; \omega) = \widehat{P3}_t e^{i(\omega t - k_3 x)} \qquad (2.5)$$

10

$P1_i(x, t; \omega), P1_r(x, t; \omega), P2_t(x, t; \omega), P2_r(x, t; \omega), P3_t(x, t; \omega)$ represent each incident, reflected, and transmitted wave in each domain. $\widehat{P1}_i, \widehat{P1}_r, \widehat{P2}_t, \widehat{P2}_r, \widehat{P3}_t$ represent the complex pressure amplitudes for each wave. The same holds for particle velocities $U1_i(x, t; \omega), U1_r(x, t; \omega), U2_t(x, t; \omega), U2_r(x, t; \omega), U3_t(x, t; \omega)$ and their corresponding complex amplitudes $\widehat{U1}_i, \widehat{U1}_r, \widehat{U2}_t, \widehat{U2}_r, \widehat{U3}_t$ (which otherwise have the same form as Equations (2.1 - (2.5). The variable ω is the angular frequency, $k = \frac{\omega}{c} = \frac{2\pi f}{c}$ is the wavenumber of each wave in its respective domain, and c is the pressure wavespeed in each respective media. The interface conditions at x = 0 and x = L require the pressure P and particle velocity U to be equal on both sides of the interface. For $x = 0$, the interface condition equations are:

$$P1_i + P1_r = P2_t + P2_r \tag{2.6}$$

$$U1_i + U1_r = U2_t + U2_r \tag{2.7}$$

Substituting Equations (2.1 - (2.5) into (2.6 - (2.7) applying $x = 0$, and combining like terms gives:

$$\widehat{P1}_i + \widehat{P1}_r = \widehat{P2}_t + \widehat{P2}_r \tag{2.8}$$

$$\widehat{U1}_i + \widehat{U1}_r = \widehat{U2}_t + \widehat{U2}_r \tag{2.9}$$

At $x = L$, the interface condition equations are:

$$P2_t + P2_r = P3_t \tag{2.10}$$

$$U2_t + U2_r = U3_t \tag{2.11}$$

Similarly, substituting Equations (2.1 - (2.5) into (2.10 (2.11), applying $x = L$, and combining like terms gives:

$$\widehat{P2}_t e^{i(-k_2 L)} + \widehat{P2}_r e^{i(k_2 L)} = \widehat{P3}_t e^{i(-k_3 L)} \tag{2.12}$$

$$\widehat{U2}_t e^{i(-k_2 L)} + \widehat{U2}_r e^{i(k_2 L)} = \widehat{U3}_t e^{i(-k_3 L)} \tag{2.13}$$

The specific acoustic impedance $z = \pm \frac{P}{U}$ is substituted into these equations where the positive and negative sign indicates a forward and backward traveling wave, respectively. This gives Equations (2.14 (2.15):

$$\frac{\widehat{P1}_i + \widehat{P1}_r}{\widehat{P1}_i - \widehat{P1}_r} z_1 = \frac{\widehat{P2}_t + \widehat{P2}_r}{\widehat{P2}_t - \widehat{P2}_r} z_2 \tag{2.14}$$

$$\frac{\widehat{P2}_t e^{i(-k_2 L)} + \widehat{P2}_r e^{i(k_2 L)}}{\widehat{P2}_t e^{i(-k_2 L)} - \widehat{P2}_r e^{i(k_2 L)}} z_2 = z_3 \tag{2.15}$$

Combining equations (2.14 -(2.15) gives the reflection coefficient as the ratio between reflected and incident waves in the first media:

$$\boldsymbol{R} = \frac{\widehat{P1}_r}{\widehat{P1}_i} = \frac{\left(1 - \frac{z_1}{z_3}\right) cos k_2 L + i \left(\frac{z_2}{z_3} - \frac{z_1}{z_2}\right) sin k_2 L}{\left(1 + \frac{z_1}{z_3}\right) cos k_2 L + i \left(\frac{z_2}{z_3} + \frac{z_1}{z_2}\right) sin k_2 L} \tag{2.16}$$

It can be seen from this equation that the reflection coefficient is dependent on the wavenumber k_2 which gives the reflection coefficient a frequency-dependent behavior. It is worth noting here that the surrounding layers also influence this calculation with the inclusion of the z_1 and z_3 terms, however, they do not impart a frequency-dependent characteristic and thus only affect the amplitude of $\boldsymbol{R}$. In Figure 4, the reflection coefficient was calculated for 1 mm thick aluminum 2024 and stainless-steel 321 plates across a frequency range spanning the first two through-thickness resonances. The material properties used in this calculation are seen in Table 1. It should be noted that this has assumed fluid media, where a solid media would use stresses instead of pressure. This analysis is identical for solid media and results in the same reflection coefficient equation.
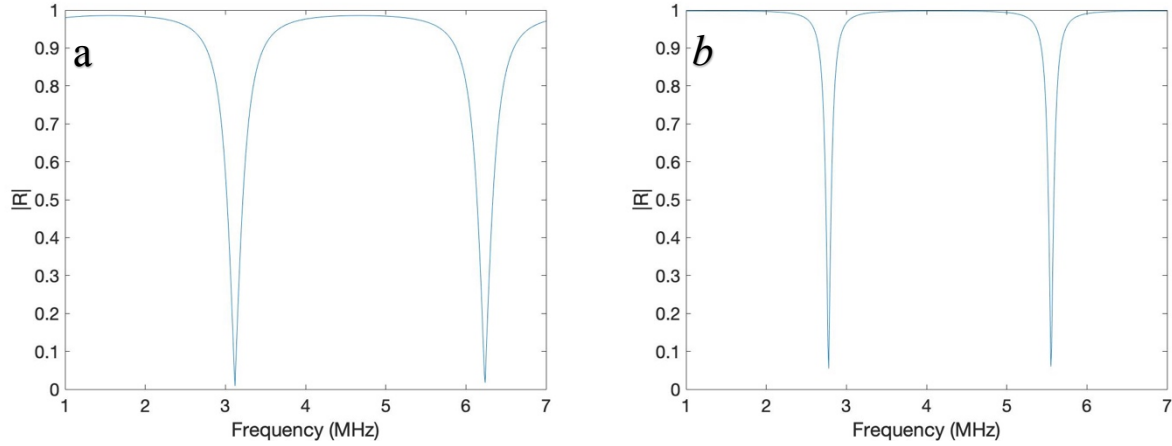
Figure 4: (a) Analytical reflection coefficient for 1mm thick aluminum 2024. (b) Analytical reflection coefficient for 1mm thick stainless steel 321

Table 1: Material properties used in the single-layer analytical

Material	Aluminum 2024	Stainless Steel 321	Water
Density (kg/m³)	2780	8000	1000
Pressure Wave Speed (m/s)	6237	5553	1480
Characteristic Acoustic Impedance (Pa·s/m³)	17.33×10^9	44.42×10^9	1.480×10^9

From these plots, sharp minima are seen at 2.78 and 5.55 MHz in aluminum and at 3.12 and 6.24 MHz in stainless steel. These frequencies are the first and second through-thickness resonances for each material, respectively. At these frequencies, the wavelength of the incident pressure wave is a half-integer multiple of the thickness of the plate, causing it to transmit fully through the material, giving the reflection coefficient a minimum value. This relationship between thickness and incident wavelength can be used to calculate which frequencies that a resonance is expected for a single layer material, seen in Equation (2.17), where c is the wave speed of the material, L is the layer thickness, and n is an integer number. Using the pressure wave speed values

13

in Table 1, Equation (2.17) will give the same resonance frequencies as predicted by the analytical model in (2.16).

$$f_{resonance} = \frac{n * c}{2L} \tag{2.17}$$

Changes in thickness or material properties will change this characteristic wavelength and thus the location of these through-thickness resonance frequencies. This can be seen in how the aluminum and stainless-steel specimens have different resonance frequencies despite being the same thickness. The aluminum, with a higher c than stainless steel, has its first resonance at a higher frequency than in the stainless steel. Observing changes in these resonances can thus provide insight into changes within the specimen itself. A downward shift in resonance location would indicate either an increase in thickness L or a decrease in wave speed c.

This is the basic concept that will be used in the inspection of lithium metal batteries; by measuring through-thickness resonances of the battery, we can infer internal changes within the battery. As mentioned before, lithium metal batteries are complex multi-layer systems in which there is no nontrivial analytical solution and thus no one-to-one correspondence between layer properties and resonance frequencies, such as in this single layer case. Another solution method is required. For this work, a numerical FEM model was used. As shown in the next section, a single layer numerical model was created and verified using COMSOL, prior to extension to multilayer models.

2.3 **Numerical Modeling**

Using the same layout seen in the previous section and seen in Figure 5, a 2D plane strain COMSOL model was constructed for a pulse-echo frequency domain inspection. It is worth

mentioning that this model was based on a well-validated model in the COMSOL Application's Library to measure the poroelastic reflection coefficient of an ocean seabed [29-30], although significant changes were made to fit the needs of this inspection approach.
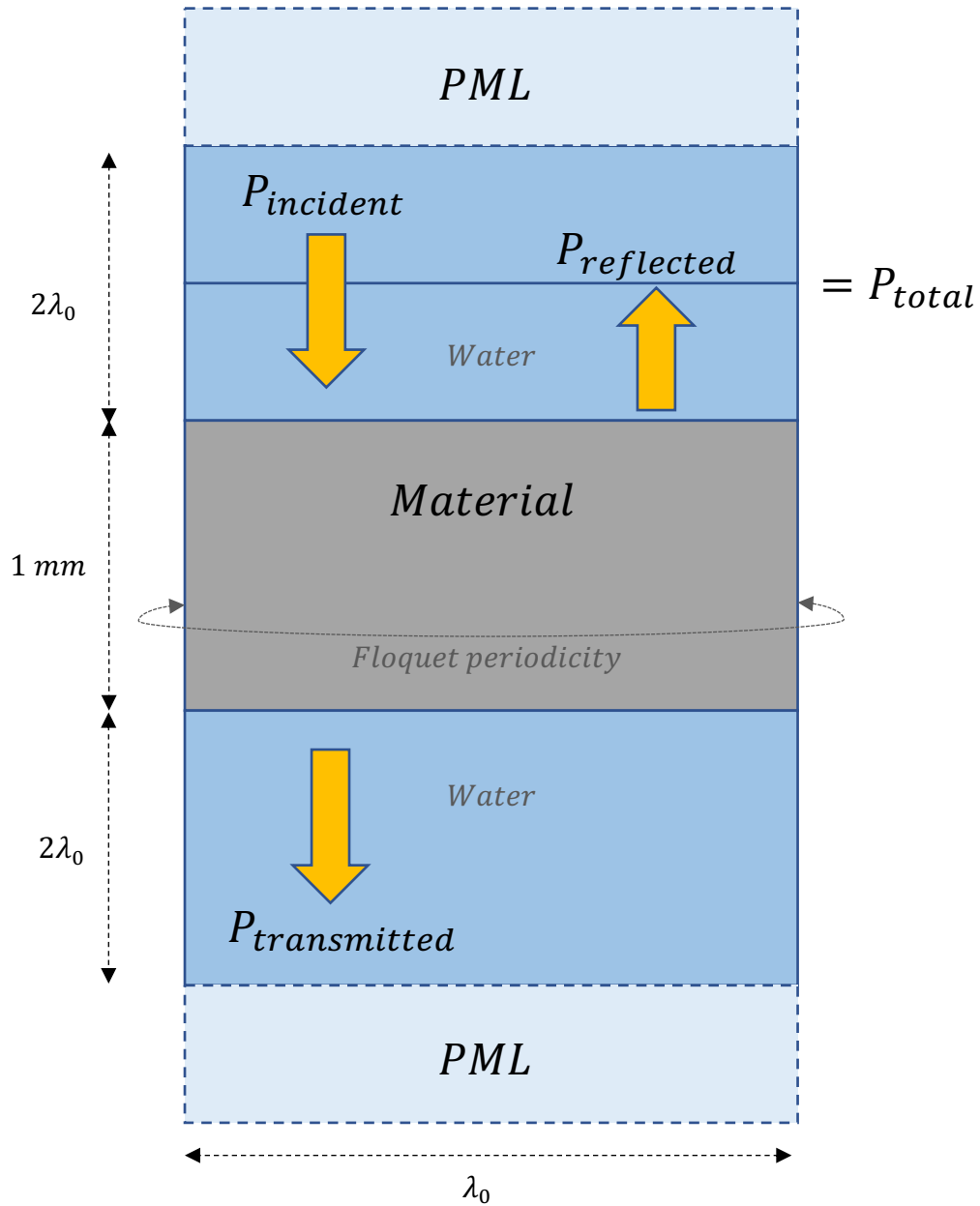

Figure 5: Layout for single layer COMSOL models. Floquet periodic conditions are used on the left and right boundaries, and perfectly matched layer (PML) boundary conditions were used on the top and bottom boundaries

In this model, a pressure wave of the form $P_{incident} = \widehat{\boldsymbol{P}}_i e^{-i(\mathbf{k}\cdot\boldsymbol{x})}$ is incident from the water domain onto a 1 mm thick material (in this case aluminum 2024 and stainless-steel 321) submerged in water where $\mathbf{k} = k_0(sin\theta_0, cos\theta_0)$, $k_0 = \frac{\omega}{c}$, and $\mathbf{x} = (x, y)$. The incident angle, θ_0, is zero in this case. The model sweeps over a specified frequency range, with the frequency of the incident wave changing each iteration, and the reflected waves are measured to obtain a reflection spectrum for the system.

This model calculates the reflection coefficient using a scattered field formulation in which the incident wave ($P_{incident}$) is a background pressure field and the total pressure measured (P_{total}) is a superposition of this background field and any reflections ($P_{reflected}$). This total pressure is measured and averaged across a line in the far-field indicated by P_{total} in Figure 5, which is sufficiently far away from any interfaces to avoid evanescent wave interference. The reflected pressure wave is calculated by subtracting the incident pressure wave from the measured total as seen in (2.18).

$$P_{reflected} = P_{total} - P_{incident} \tag{2.18}$$

The reflection coefficient is then calculated using Equation (2.16). Plots of reflection coefficients for 1 mm thick aluminum 2024 and stainless steel 321can be seen in Figure 6.

The left and right boundary conditions are modeled using Floquet periodicity, which simulates the observed unit cell repeating periodically in the x-direction [31-32]. Perfectly matched layer (PML) boundary conditions were used for the top and bottom boundaries, which simulate absorbing boundaries in which incident waves will not reflect [33]. The x-dimensional width was set to be equal to one wavelength of the incident pressure wave, which will change for each

iteration of the model. The height of the water domains was set to be double this wavelength to ensure that one entire wavelength at minimum could propagate through this domain. In addition, the mesh size of the water domains was set to have ten elements per wavelength in both the x and y-directions, scaling with the frequency of the incident wave. The plate domain was set to have 5 quadratic elements per thickness in the y-direction and the same discretization as the water domain in the x-direction. This ensures sufficient spatial discretization at all frequencies across the entire model.

This model uses a 2D plane-strain assumption, and is solved in the frequency domain. Acoustic-structure multiphysics coupling is used at the interfaces between the plate and water domains. The material properties used as inputs for this model can be seen in Table 2.

Table 2: Material properties used for single layer plate models

Material	Aluminum 2024	Stainless Steel 321
Density (kg/m³)	2780	8000
Elastic Modulus (GPa)	73.0	193
Poisson Ratio	0.33	0.28
Pressure Wave Speed (m/s)	6237	5553

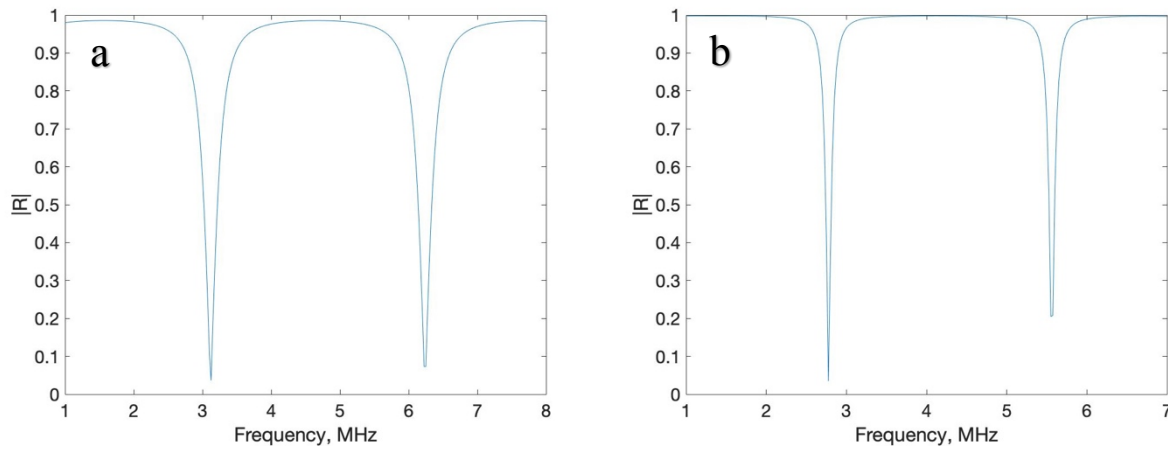*Figure 6: Numerical reflection coefficients for (a) aluminum 2024 and (b) stainless steel 321*

Table 3: Results from analytical and numerical models

| Material	Analytical		Numerical	
	First Resonance	Second Resonance	First Resonance	Second Resonance
Stainless Steel 321	2.78 MHz	5.55 MHz	2.78 MHz	5.55 MHz
Aluminum 2024	3.12 MHz	6.24 MHz	3.12 MHz	6.24 MHz

From these plots, the numerical simulation matches the analytical model's predicted resonance frequencies for both materials. This gives confidence in the model implementation and setup for building up into cases with multiple layers. In the next section, an experimental setup is used to validate the results from both models.

2.4 Pulse Echo Measurements

2.4.1 Experimental Setup

To validate the results from these models, pulse-echo measurements were performed to calculate the reflection coefficient for 1mm thick plates of aluminum 2024 and stainless steel 321. A 3.5 MHz Panametrics V682 delay line transducer is used with a Panametrics 5072 Pulser-Receiver to perform the inspections. The delay line is required to isolate the excitation signal from the specimen's reflections. Soundsafe® ultrasonic couplant was used to couple the surface of the delay line to the surface of the metal plate, and a 2 kg weight was placed on top of the transducer

to apply constant pressure and ensure a flat coupling interface. A picture of the experimental setup can be seen in Figure 7.
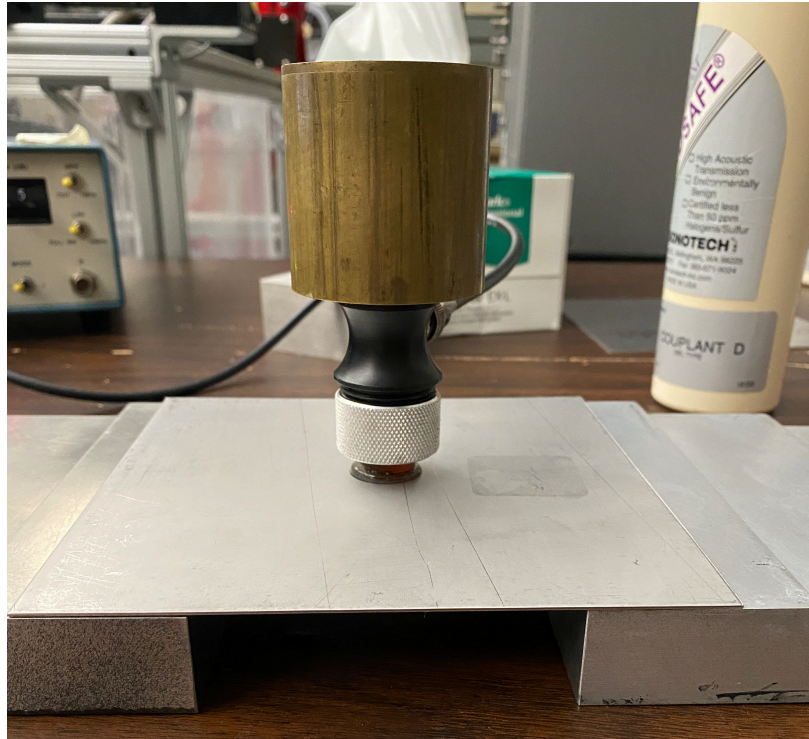
Figure 7: Delay Line transducer coupled to stainless steel plate

2.4.2 Reflection Coefficient Extraction - Linear Systems Deconvolution

To calculate the reflection coefficient with this setup, the signal from the inspected specimen must be isolated from the other contributing responses of the setup (delay line,

electronics, etc.). This can be done by taking a linear systems approach and assigning transfer functions to the components in the system. A diagram of this is seen in Figure 8.
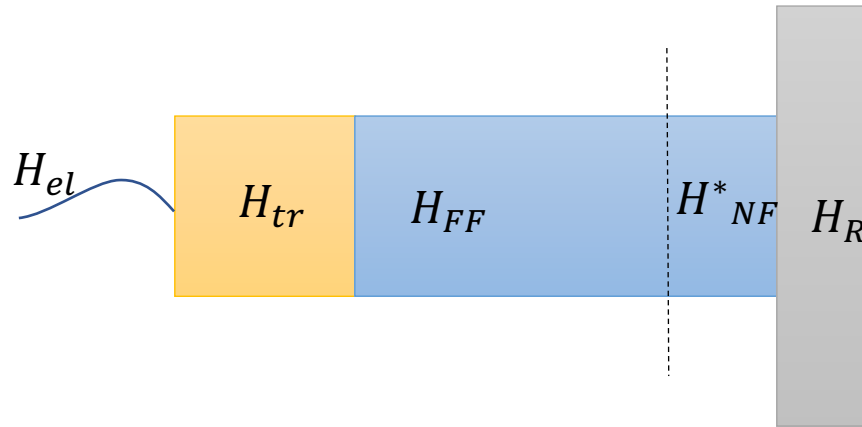

Figure 8: Pulse echo delay line inspection setup

In this setup, H_{el}, H_{tr}, H_{FF}, H_{NF}, and H_R account for the transfer functions of the electronics, transducer, delay line, and the inspected specimen, respectively. The subscript in H_R is for reflection, emphasizing that this setup provides a reflection coefficient for the entire specimen. The delay line has been split up into two separate transfer functions H_{FF}, and H_{NF} representing the far-field and near-field portions of the delay line, respectively. This distinction is made to isolate the near field effects at the specimen/delay line interface (i.e., influence of evanescent modes), and because reflection coefficients are by definition measured in the far-field. If not accounted for, near-field effects can contribute spurious artifacts to the post-processed battery response. An input voltage is used for the system input, which excites a pressure wave on the transducer's face (H_{tr}) that travels through the delay line (H_{FF}, H_{NF}). The ultrasonic wave resonates locally within the specimen (H_R) via a multitude of transmissions and reflections, then propagates back through the delay line, is converted back to an electrical signal by the transducer and receiving electronics, and then is recorded as V_{out}. The transfer function relationship for this output voltage can be described by Equation (2.19) below.

$$(V_{out})_R = V_{in} \times H_{el} \times H_{tr} \times H_{FF} \times H^*_{NF} \times H_R \times H^*_{NF} \times H_{FF} \times H_{tr} \times H_{el} \qquad (2.19)$$

The specimen's reflected transfer function, H_R, is the variable that needs to be isolated. By taking a measurement with the specimen (H_R) removed, we get a similar expression to (2.19). H'_{NF} here represents a different interface condition from H^*_{NF} when no specimen is coupled. Figure 9 shows this setup and its associated transfer function relationship is in Equation (2.20).
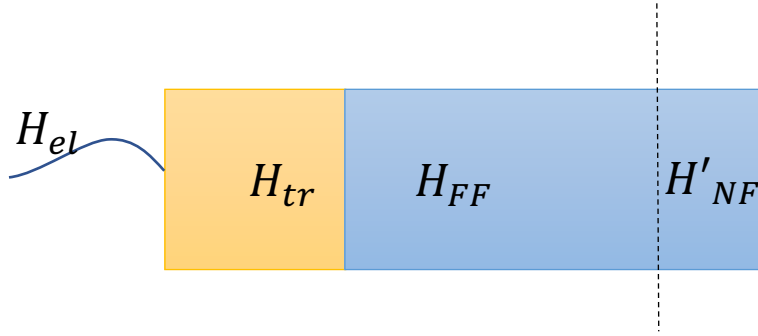

Figure 9: Delay line ultrasound inspection calibration setup

$$(V_{out})_{cal} = V_{in} \times H_{el} \times H_{tr} \times H_{FF} \times H'_{NF} \times H'_{NF} \times H_{FF} \times H_{tr} \times H_{el} \qquad (2.20)$$

With these two relationships, the calculation $\frac{(V_{out})_R}{(V_{out})_{cal}}$ can be taken will give the reflection coefficient $\boldsymbol{R}(\omega)$:

$$|\boldsymbol{R}(\omega)| = \frac{|(V_{out})_R|}{|(V_{out})_{cal}|} = |H_{NF}| \times |H_R| \times |H_{NF}| \qquad (2.21)$$

Two H_{NF} are left after this calculation, which is associated with any near field effects at the edge of the H_{NF} interface. These terms are the ratio of the two near field terms $\frac{H^*_{NF}}{H'_{NF}}$, and were combined into H_{NF} for simplicity of analysis. This will influence the amplitude of the reflection

21

coefficient but won't alter the location of any resonance frequencies. This is demonstrated in Figure 4, where the two different materials have different amplitude characteristics in addition to resonances. The aluminum reflection coefficient is lower in amplitude and wider resonance minima, while the stainless-steel reflection coefficient has a higher amplitude and sharper minima. These differences are attributed to these near-field contributions from the differing acoustic impedances. Also, the different boundary conditions at the end of the delay line in the calibration setup will create a phase difference in the H_{NF} term. Thus, the absolute value of the two V_{out} terms must be taken so that only the magnitudes are incorporated in the calculation.

For this linear systems approach to work, each individual component must be behaving linearly. The electronics and transducer used throughout this work were checked for linearity by performing the described deconvolution approach at different energy/amplitude settings on the pulser-receiver. The scaling of input voltage produced a corresponding scaling of the output voltage across the entire frequency spectrum used in these measurements, confirming that these components are behaving linearly.

2.5 Results: Model Validation

2.5.1 Delay Line Experiments

With this method established, it can be validated with an inspection of the metal plates used in the modeling. Figure 10 Figure 11 show the reflected waveforms for the metal plates and free transducer. Because the use of a delay line causes multiple reflections within itself, these figures have been windowed to only include the delay line's first reflection.
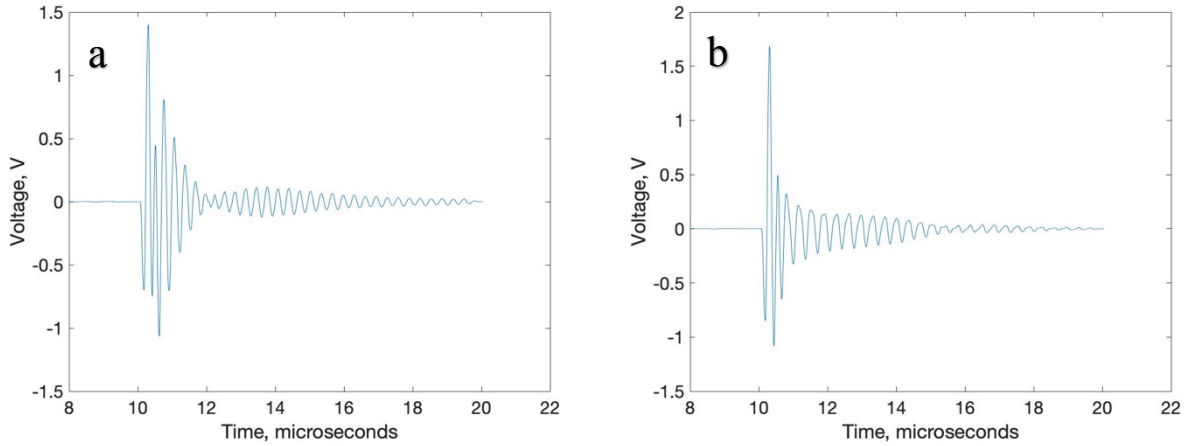
Figure 10: Time-domain data from 1mm thick (a) aluminum 2024 and (b) stainless steel 321 delay line inspections
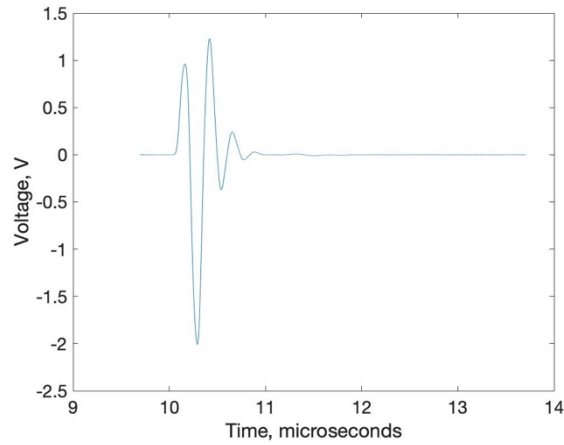

Figure 11: Time-domain data for the free delay line transducer in air

The Fast-Fourier Transform (FFT) was then performed on each of these signals to get data in the frequency domain. To prevent spectral leakage when computing the Fourier transform, it is important to let the reflections decay down to zero. In this case, the second delay line reflection occurred before this ringdown could completely finish, so a Tukey window with a cosine fraction of 0.1 was applied to the waveforms before performing the FFT. The magnitudes of the FFT can be seen in Figure 12 and Figure 13. Resonances can be seen in these plots already, but this data still includes the transducer response, so it is not isolated yet. Figure 12 and Figure 13 represent

Equations (2.19) and (2.20), respectively, in this sense. Using Equation (2.21), we can calculate the reflection coefficients for each of the metal plate specimens, which is shown in Figure 14.
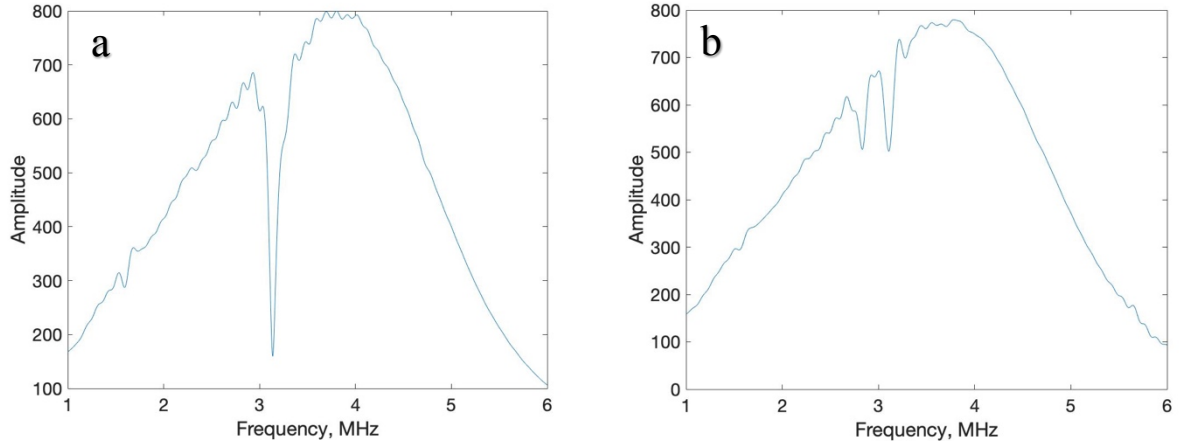

Figure 12: FFT data from 1mm thick (a) aluminum 2024 and (b) stainless steel 321 delay line inspections
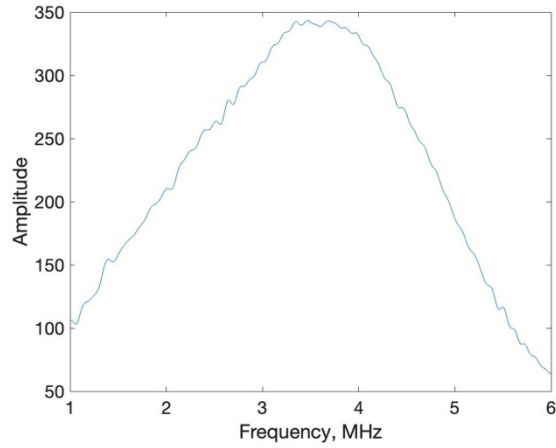

Figure 13: Frequency domain data from the free 3.5 MHz delay line transducer
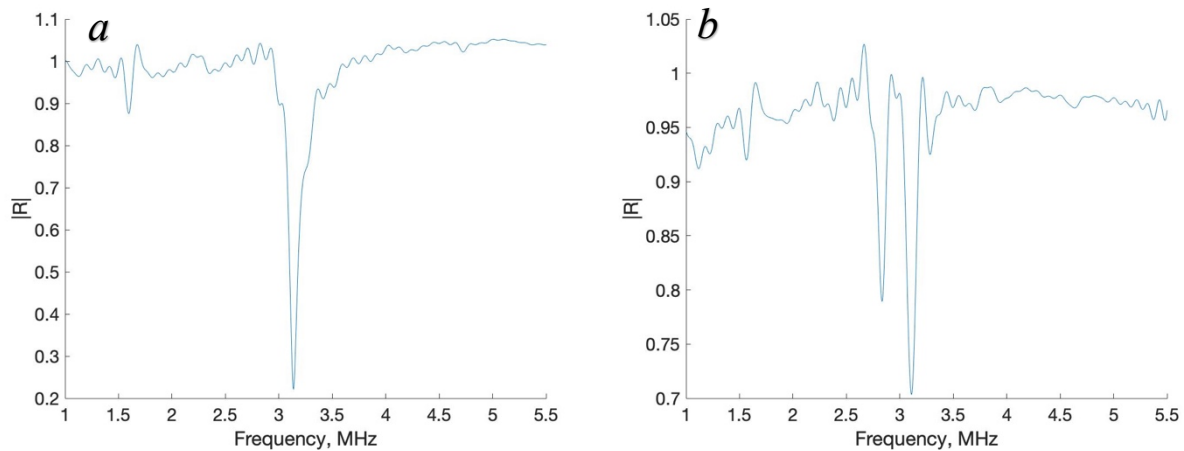
Figure 14:Frequency domain data from 1mm thick (a) aluminum 2024 and (b) stainless steel 321 delay line inspections

Table 4: Predicted resonance frequencies versus measured resonance

Material	Predicted Resonance	Measured Resonance
Stainless Steel 321	2.78 MHz	2.83 MHz, 3.11 MHz
Aluminum 2024	3.12 MHz	3.14 MHz

From the plots in Figure 14 and data in Table 4, resonances can be seen at 2.83 and 3.11 MHz for the stainless steel and at 3.14 MHz for the aluminum. The model predicted resonance is present, however, there are unexpectedly extra resonances in the results. The stainless-steel shows two separate resonances around 3 MHz, and even a small resonance is present around 1.5MHz in both specimens.

These extra resonances are hypothesized to be due to shear wave mode conversion from a slight tilt in the specimens/setup. Mode conversion such as this will occur whenever a pressure wave is incident on an interface at an oblique angle. This is demonstrated in Figure 15. The angle

of refraction for each of these wave modes can be explained by Snell's Law in Equation (2.22). If the incident pressure wave is incident at a slight angle, a small amount of shear wave modes will be generated, and every subsequent internal reflection will cause more accumulation of shear modes. Since time windows are taken for these signals, there are many opportunities for this mode conversion to occur.
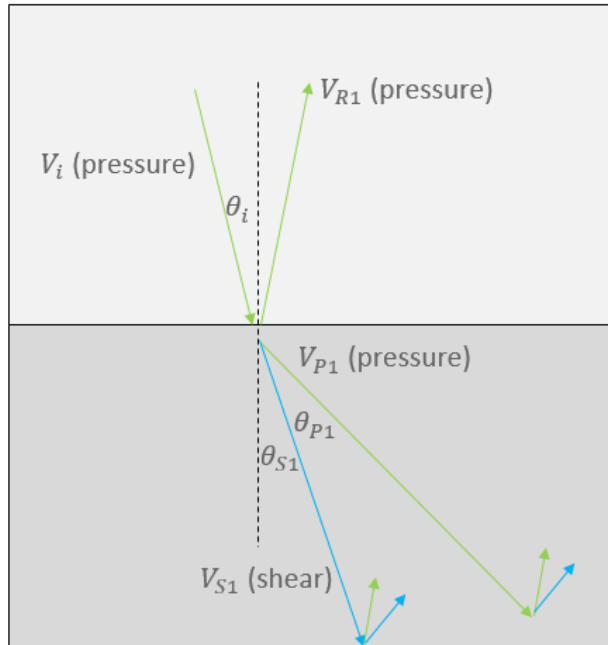

Figure 15: Shear wave mode conversion will occur from an incident pressure wave at a slight angle

$$Snell's\ Law = \frac{\sin\theta_i}{V_i} = \frac{\sin\theta_{S1}}{V_{S1}} = \frac{\sin\theta_{P1}}{V_{P1}} \tag{2.22}$$

In addition, Equation (2.17) can be used to calculate shear mode resonances by using the shear wave speed as c instead of the pressure wave speed. For aluminum 2024, this speed is 3141 m/s and gives shear wave resonances at 1.57 and 3.14 MHz. This lines up very well with Figure 14, and indicates that the 3.14 MHz is most likely a superposition of shear and pressure resonances. For stainless-steel 321, the shear wave speed is 3069 m/s and gives shear resonances at 1.53 and

3.07 MHz. This indicates that the extra resonance observed at 3.11 MHz in the experimental data is due to a shear wave resonance.

To confirm that this is what is happening, submerged water tank inspections were performed on each specimen. Since shear waves cannot travel through fluid media, observing these resonances in a submerged inspection will corroborate this explanation.

2.5.2 Submerged Water Tank Inspections

Submerged water tank inspections were performed for both the 1mm aluminum 2024 and stainless steel 321 specimens using a 5 MHz Panametrics V309 transducer and a Panametrics 5072 Pulser-Receiver. These inspections were performed as scans, so multiple data points were aligned via their maximum cross-correlation, then averaged together to get the reflection spectra. The deconvolution approach for these scans is similar to that of the contact transducer inspections, except that the transducer calibration data was taken from the front surface reflections from a flat stainless-steel block. To account for the reflection off the stainless-steel block, there is also a scalar factor of 0.87 multiplied to the measured reflection spectra. This factor is the analytical reflection coefficient for a water/stainless-steel interface. The results from these inspections can be seen in Figure 17 and in Table 5.
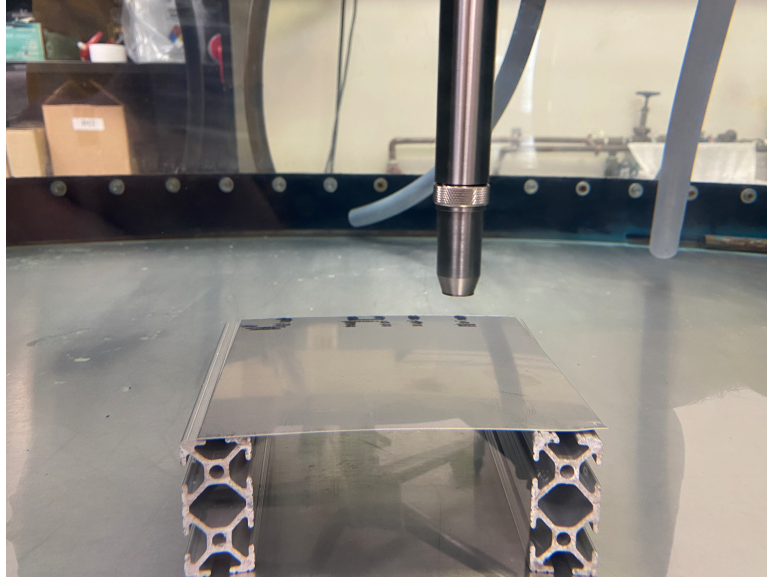
Figure 16: Submerged water tank inspection on stainless steel and aluminum plates
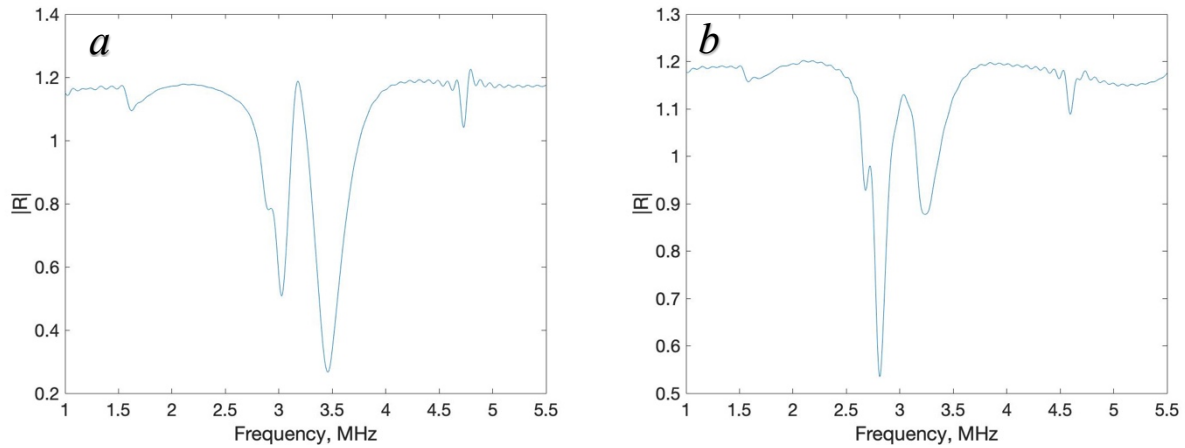

Figure 17: Reflection coefficients for (a) aluminum 2024 and (b) stainless steel 321 in a submerged water tank

inspection

Table 5: Results from water tank inspections

Material	Water Tank	
	Pressure Resonance	Shear Resonance
Stainless Steel 321	2.81 MHz	3.23 MHz
Aluminum 2024	3.01 MHz	3.45 MHz

Multiple resonances can once again be seen in these plots, where only one is expected. The stainless-steel reflection coefficient shows a pressure and shear resonance, as seen before in the experimental results. The pressure resonance is still in the same location, while the shear resonance has shifted upward slightly. The aluminum reflection coefficient shows two separate resonances around 3 MHz, which was not seen in the previous results. Checking the time of flight across the entire scan showed that the specimens were at approximately a 1-degree angle, most likely due to slightly uneven supports. This angle is probably greater than what was present in the previous contact inspections, which could explain why there are two separate resonances in the aluminum, as the two wave modes will experience slightly different thicknesses and thus resonances at different angles. This could also explain the slight shift in stainless-steel resonances.

These extra resonances were not seen in the previous modeling results, since the incident wave was modeled as entirely perpendicular to the specimen. To determine whether the model can accurately predict the experimentally observed mode conversion, the model from Section 2.2.2 was run again with the incident wave tilted by one-degree. Figure 18 shows the reflection coefficients for aluminum and stainless steel from the model with this adjustment. Table 6 shows

the locations of the resonances and compares them with the experimental results. Table 7 shows the percent error in resonance location between the two results.
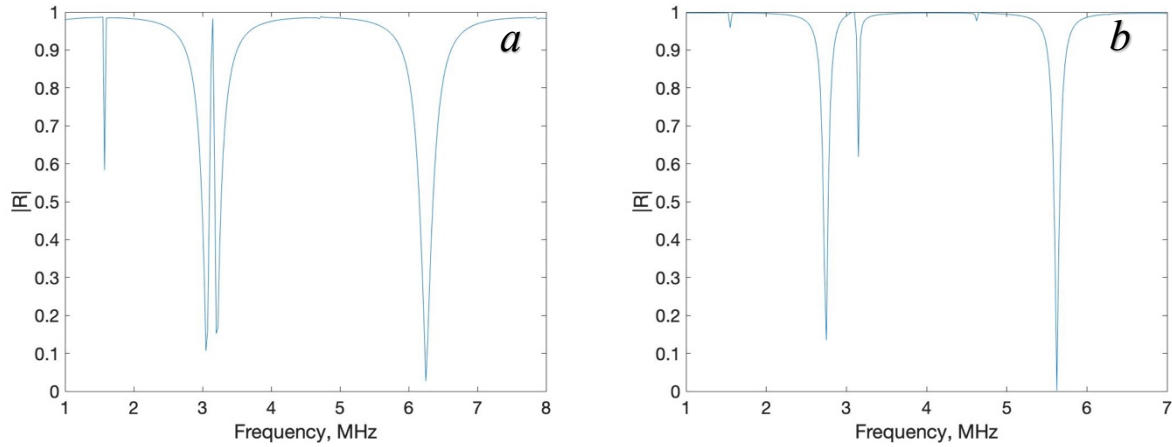

Figure 18: Numerical reflection coefficients for (a) aluminum 2024 and (b) stainless steel 321 at a 1-degree tilt

Table 6: Comparison between experimental and simulated results

Material	Numerical – 1-degree tilt		Experimental Water Tank	
	Pressure Resonance	Shear Resonance	Pressure Resonance	Shear Resonance
Stainless Steel 321	2.75 MHz	3.15 MHz	2.81 MHz	3.23 MHz
Aluminum 2024	3.05 MHz	3.2 MHz	3.01 MHz	3.45 MHz

Table 7: Percent error in resonance location between experimental and modeling results

Material	Percent Error between Modeling and Experiments	
	Pressure Resonance	Shear Resonance
Stainless Steel 321	2.18%	2.54%
Aluminum 2024	-1.31%	7.81%

The two results match very well, with a maximum error of 7.81% between modeling and experiment for aluminum shear resonance, and the other resonances all under 3% error. With this, the basic workings of the pulse-echo inspection technique have been demonstrated. The reflection coefficient will exhibit minima at the resonance frequencies of the inspected specimen. These resonances are dependent on the material properties of the specimen, as shown with the reflection spectra changing between the two different materials.

In addition, shear wave mode resonances were seen due to internal mode conversion in the specimen. This finding added significant challenges to the interpretation, prompting reassessment of the experimental techniques, as well as the need to cross-validate in simulation. After the appropriate checks were performed, the work of Guyott and Cawley [34] was found which demonstrated the phenomena of pressure-to-shear mode conversion in through-thickness resonance inspection of metal plates. Although they proved the existence of this phenomena, their results still included the response of the measurement system (transducer, electronics, etc.). In the present work, by isolating the specimen's response, a more detailed assessment of the magnitude and impact of this phenomena is obtained. Furthermore, the FEM modeling provides a robust foundation for exploring this behavior – which to date has received little note – in more complex systems. In the next section, this technique is used to inspect lithium metal batteries.

Chapter 3: Local Ultrasound Spectroscopy of Lithium Metal Batteries

3.1 **Experimental Approach and Setup**

With this technique established, it was then applied for the inspection of a lithium metal battery. The goal of these inspections is to identify signal features pertaining to battery defects. Thus, inspecting both clean and defective batteries is necessary to establish this correlation. To mimic lithium plating defects, ~80μm thick lithium chips of varying diameters were embedded onto the battery anode, as seen in Figure 19. These defects are very coarse, but this is desirable for establishing the efficacy of the technique with a battery inspection. These batteries were manufactured and provided by Cornerstone Research Group.

With this, the reflection coefficient can be measured at a defect region on the battery and compared with the reflection coefficient from a clean region. The same experimental setup and reflection measurement procedure seen in Section 2.1 was used for this, which is shown in Figure 20. The results of the experiments are discussed next.
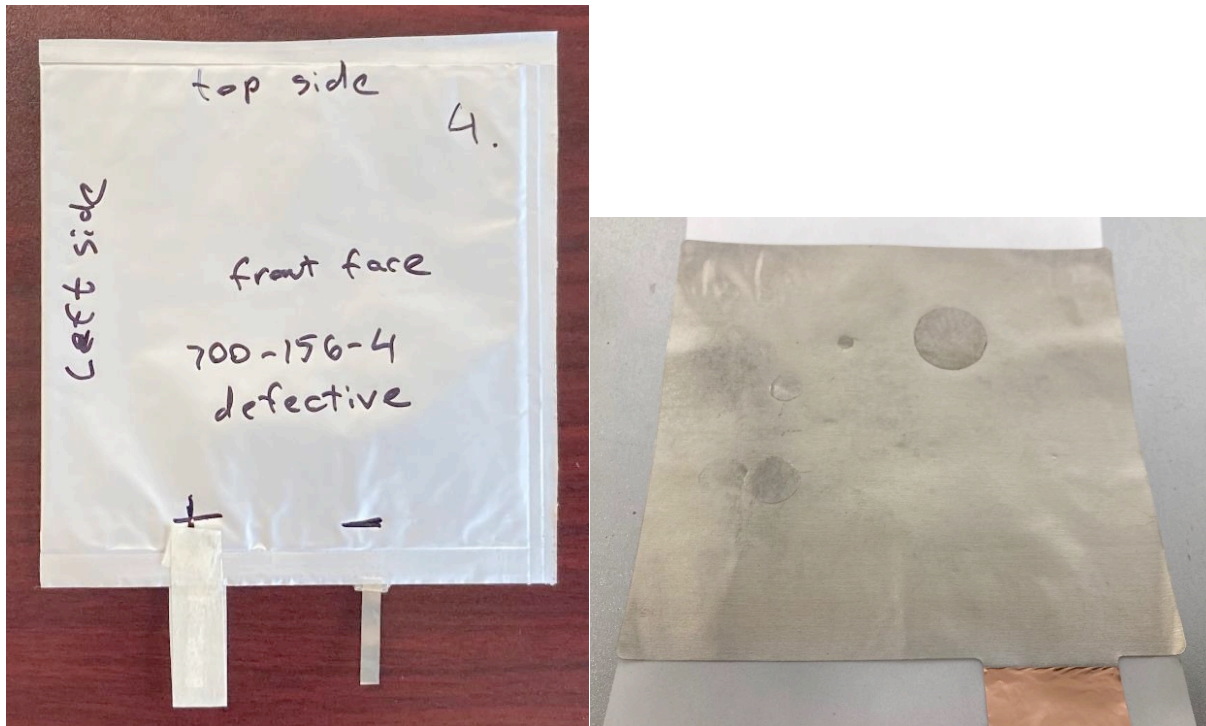
Figure 19: Image of single-cell battery. The right image shows a lithium chip defect embedded on the lithium anode
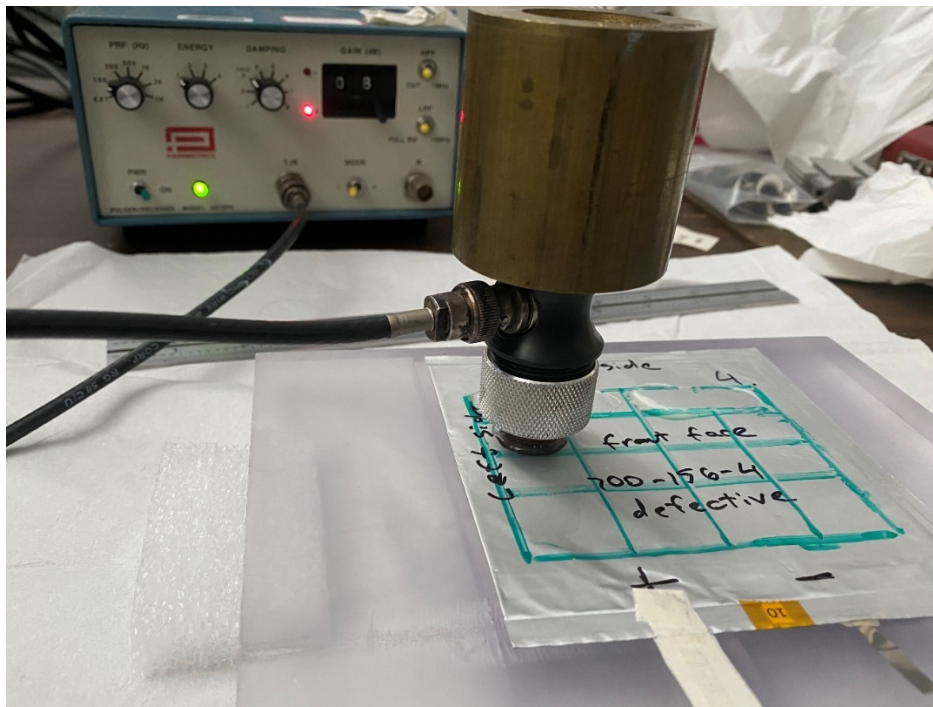

Figure 20: Lab photo of inspection on lithium metal battery

3.2 **Experimental Results**

The collected waveforms from these inspections can be seen in Figure 21. As expected, the time domain reflections from the thin layers all overlap. The clean and defective reflection coefficients were calculated with the procedure described in Section 2.3.2. Three resonances appear in the frequency range examined, with their exact values shown in Table 8. Comparing the locations of these resonances between the clean and defective regions, there is a significant downward shift in frequency when a defect is present. For a single-layered case, Equation (2.17) implies a downward resonance shift when there is an increase in layer thickness. Using this as a guideline towards the multilayered battery case, the presence of a lithium chip defect creates a local increase in thickness, so a downward shift in resonance location is expected.
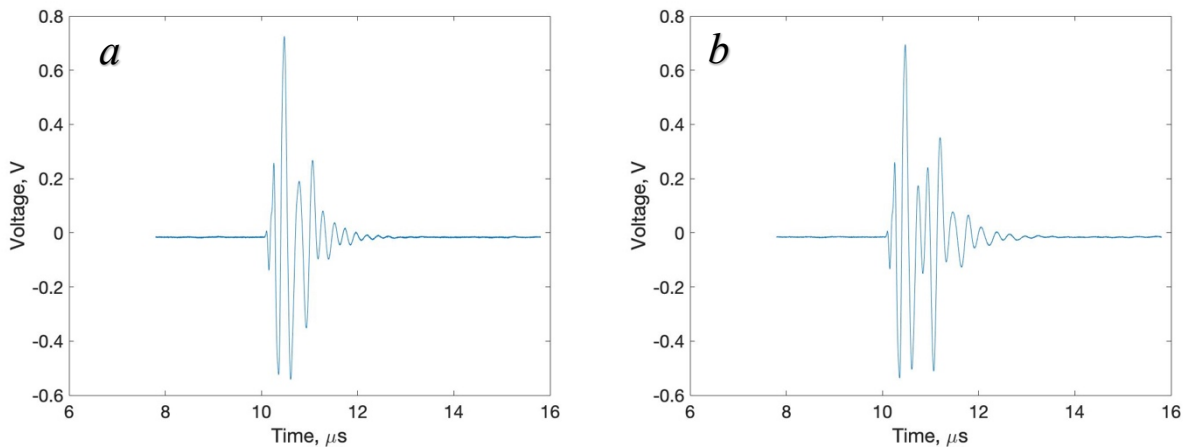
Figure 21: Time-domain plots from battery inspections. (a) shows results from a clean region, (b) show results from a defect region
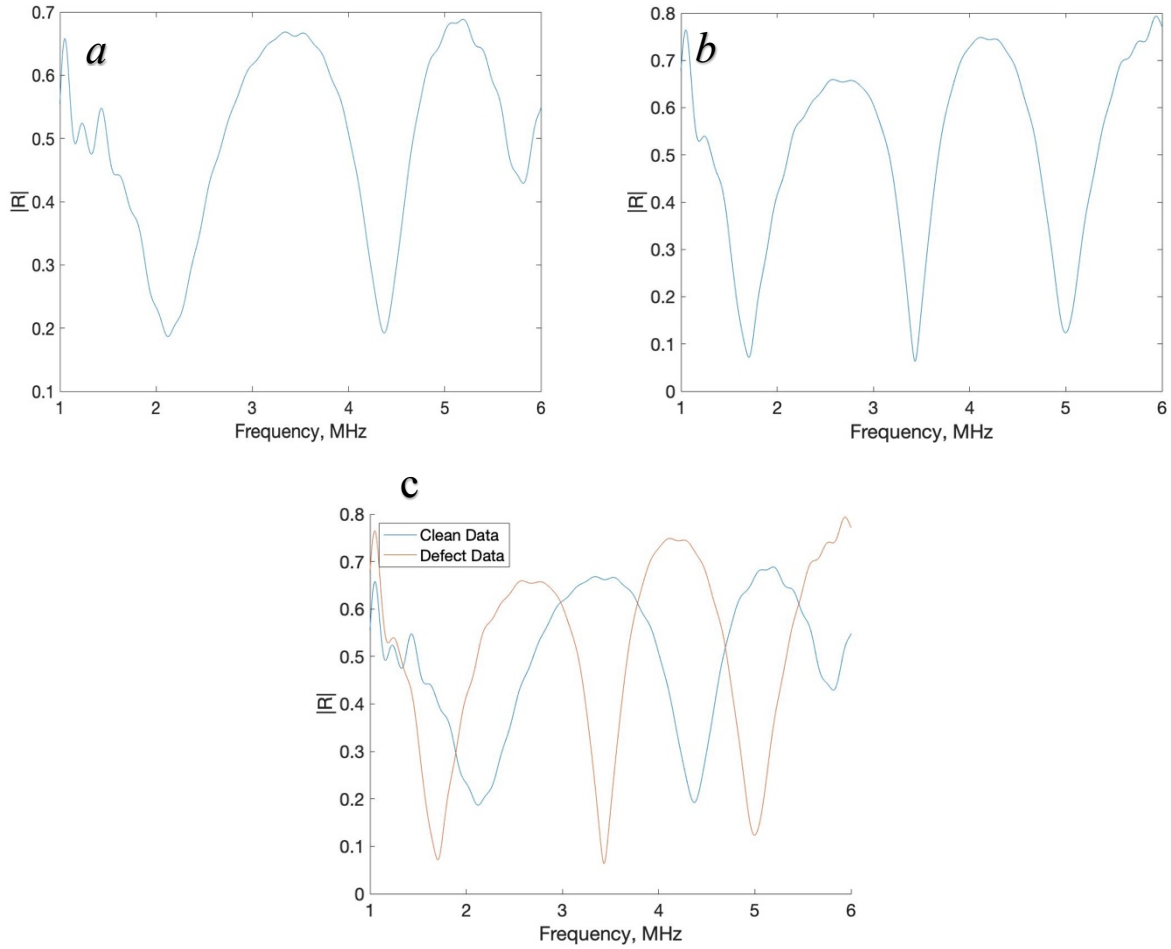
Figure 22: Reflection Coefficients for (a) clean region, and (b) defective region. (c) Shows both reflection coefficients overlaid

Table 8: Resonance frequencies determined via battery reflection coefficients

Battery Region	First Resonance	Second Resonance	Third Resonance
Clean	2.189 MHz	4.377 MHz	5.76 MHz
Defect	1.712 MHz	3.433 MHz	4.997 MHz

These inspections were performed several times, and some variance in shape and amplitudes of the measured reflection coefficient was observed. This is due to various aspects of the contact transducer technique. The thickness of the ultrasonic couplant used can vary from

35

measurement to measurement, which would have an effect on the resonances seen. A weight was placed on top of the transducer to try and minimize this, but it is still possible that slight variations occurred. In addition, the electrolyte inside the battery can disperse with the added force, adding to the experimental variance. Despite this, the resonance frequencies seemed mostly stable. Figure 23 shows the variance in measurements from the same pristine regions on the battery after recoupling to the battery.
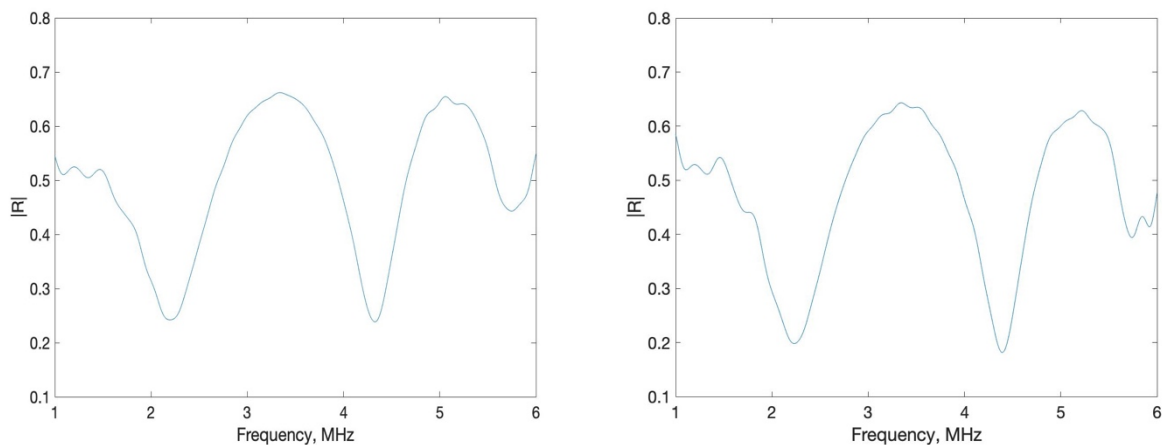
Figure 23: Variance in reflection coefficients from the same pristine battery region after coupling and recoupling

From these plots, slight variations in amplitude across the spectra can be seen. This is emphasized when looking at the y-axis scaling between plots. Further comparison with Figure 22a also emphasizes the variance observed. To quantify this variance and to also determine whether the measured resonance frequencies are stable despite amplitude variations, these measurements were repeated multiple times. The results of this are discussed in the next section.

3.2.1 Statistical Analysis of Resonance Shifts

Ten different inspections were performed on pristine regions of the battery, and ten more were performed on regions with an embedded defect. The transducer was decoupled and recoupled

to the battery before and after each measurement to re-introduce sources of experimental error, so that each measurement could be treated as independent.

Each of the three present resonances were treated as separate datasets, which can be seen in Table 9. A series of two-mean Student's t-tests were performed, comparing frequencies for the pristine and defect data for each of the first three resonances. The associated standard deviation with each resonance was very low. The p-values for each t-test were very small, each lower than 10^{-12}, indicating a statistically significant difference in mean resonance frequency for each resonance assessed.

Table 9: Results and statistics from 10 sets of reflection coefficient measurements

Trial	Resonance 1		Resonance 2		Resonance 3	
	Clean	Defect	Clean	Defect	Clean	Defect
1	2.141	1.750	4.244	3.476	5.755	5.016
2	2.132	1.693	4.268	3.438	5.617	5.007
3	2.146	1.807	4.301	3.481	5.693	5.059
4	2.146	1.779	4.292	3.529	5.732	5.069
5	2.255	1.793	4.358	3.462	5.808	5.069
6	2.155	1.750	4.310	3.429	5.808	5.045
7	2.255	1.726	4.396	3.471	5.827	5.130
8	2.222	1.769	4.392	3.471	5.746	5.050
9	2.284	1.826	4.354	3.533	5.722	5.1070
10	2.294	1.783	4.349	3.533	5.832	5.102
Mean	2.203	1.768	4.326	3.482	5.754	5.065
Std Dev	0.06532	0.03938	0.05140	0.03789	0.06765	0.03934
p-value	5.619×10^{-13}		2.224×10^{-19}		3.023×10^{-16}	

From these results, the proposed inspection technique proves to be reliable in detecting resonance shifts associated with the presence of an embedded defect representative of lithium plating in single-cell lithium metal batteries.

## 3.3 **Numerical Modeling of Lithium Batteries**

3.3.1 Model Setup

A frequency-domain model of a lithium metal battery undergoing a pulse-echo inspection was then constructed. Validating this model is important for future work in which various other defect conditions or inspection techniques could be performed.

The setup of the model is the same as with the single-layer model used in Section 2.2.2, but the battery layout is seen in Figure 24, replacing the metal plate. The full battery layout is seen in Figure 25. It can be seen from this that each battery component is comprised of three sublayers. The surrounding pouch material has a structure of oriented nylon on top, aluminum in the middle, and polypropylene on the bottom. The Celgard 2325 separator is a porous stack of polypropylene/polyethylene/polypropylene. The anode is composed of a copper current collector in between two solid lithium electrodes. Similarly, the cathode is composed of an aluminum current collector in between two porous $LiCoO_2$ electrodes. In addition, this model incorporates Biot poroelasticity, so the porous materials are filled with a $LiPF_6$ in EC:DEC:DMC electrolyte. The elastic material properties used are defined in Table 10, and the poroelastic material properties are defined in Table 11. To reduce artifacts from overly sharp resonance frequencies, a damping factor of 0.05 was implemented as an isotropic loss factor to the solid materials. This was sufficient to smooth the frequency-domain response to better identify resonance frequencies, while not being large enough to impact quantitative comparisons.

Each individual layer was set to have 5 quadratic elements per thickness along the y-direction, and scales with the wavelength in the x-direction as in the model setup for the metal plate resonance. A nominally pristine model was run, and also a model with an 80 μm lithium

defect embedded on the anode to emulate the defect conditions from the experiments. The normal

incidence reflection coefficients for clean and defect conditions are seen in Figure 26.
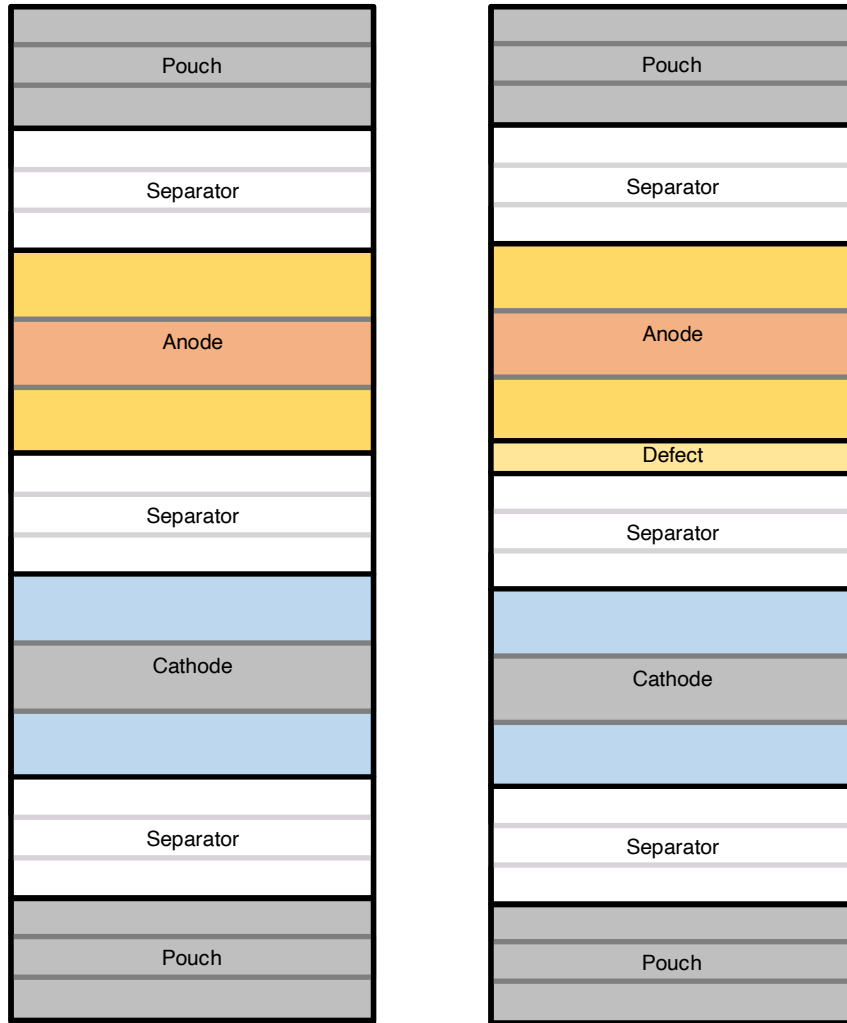
Figure 24: Single cell battery layout used for modeling. Left shows battery without defect. Right shows embedded defect on battery anode
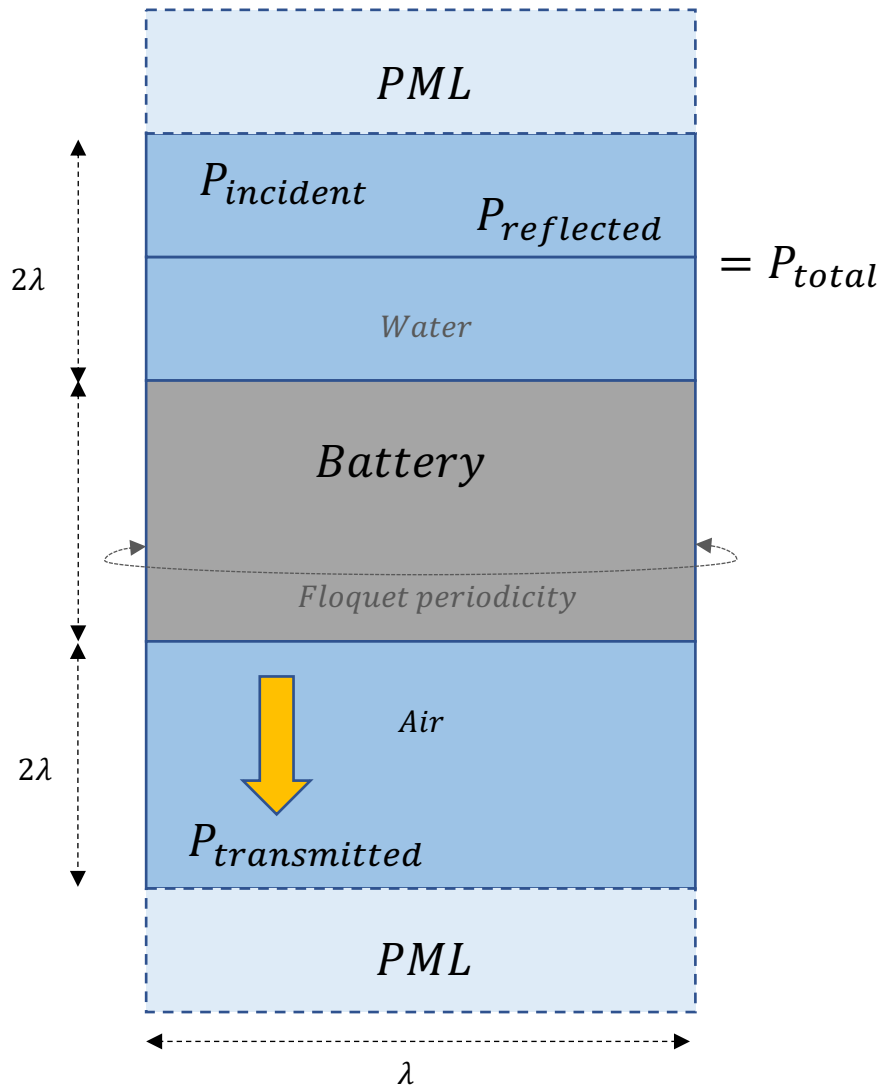
Figure 25: Model layout used for the battery model inspections

Table 10: Elastic properties used in the models

Component	Material	Thickness (μm)	Density (kg/m^3)	Young's Modulus (GPa)	Poisson Ratio
Pouch	Nylon	15	1140	2.87 [34]	0.3 [34]
	Aluminum	35	2700	70.3	0.33
	Polypropylene	36	880	4.5 [35]	0.2 [35]
Separator	Polypropylene	8.33 [36]	880	4.5 [35]	0.2 [35]
	Polyethylene	8.33 [36]	930 [37]	1.37 [37]	0.437 [37]
Anode	Lithium	50	530	7.82 [38]	0.381 [38]
	Copper	50	8940	70	0.347
Cathode	LCO	76	4790	191 [39]	0.24 [39]
	Aluminum	17	2819	70.3	0.33

Table 11: Poroelastic material properties used in the models

Component	Material	Porosity	Tortuosity	Permeability	Biot-Willis Coefficient
Separator	Polypropylene	0.39 [36]	2.27 [36]	7.22 x 10^{-7} [19]	1
	Polyethylene	0.44 [36]	2 [36]	7.22 x 10^{-7} [19]	1
Cathode	LCO	0.36 [40]	2.5 [41]	7.22 x 10^{-7} [19]	1

Table 12: Poroelastic material properties used in the models

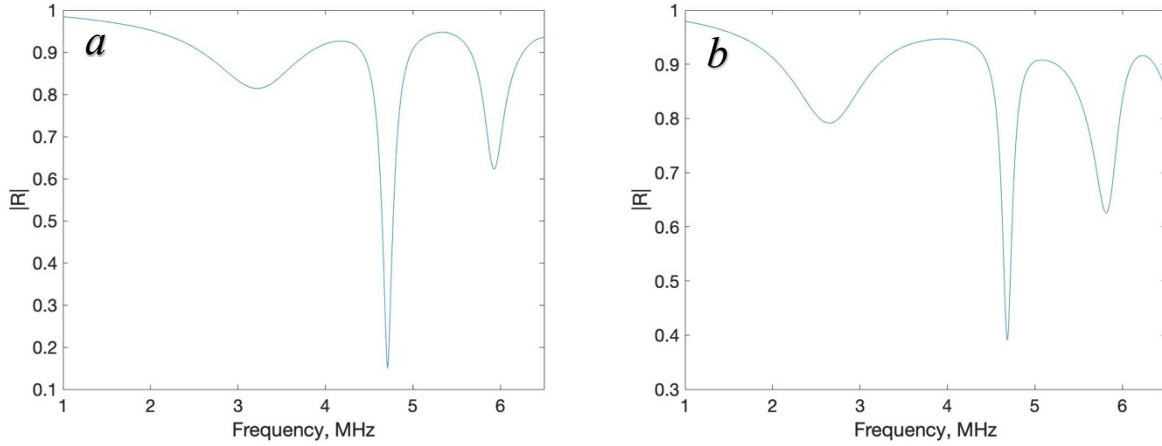| Component	Material	Density (kg/m^3)	Bulk Modulus (GPa)	Dynamic Viscosity (Pa·s)
Electrolyte	LiPF$_6$ in EC:DEC: DMC	1270 [19]	1 [19]	0.042 [19]

Figure 26: Reflection Coefficient from battery model. (a) shows clean battery condition and (b) shows a battery with embedded defect

Table 13: Resonance locations compared between modeling and experimental results

	Pristine Battery			Defect Battery		
	First Resonance	**Second Resonance**	**Third Resonance**	**First Resonance**	**Second Resonance**	**Third Resonance**
Modeling	3.2 MHz	4.71 MHz	5.93 MHz	2.65 MHz	4.68 MHz	5.81 MHz
Experimental	2.189 MHz	4.377 MHz	5.76 MHz	1.712 MHz	3.433 MHz	4.997 MHz
Error	46.19 %	7.61 %	2.95 %	54.79 %	36.32 %	18.67 %

3.3.2 Comparison with Experimental Results

Table 13 shows the numerical values of the observed resonance frequencies in Figure 26. For the pristine battery case, the second and third resonances show very low errors in terms of frequency location while the first resonance shows an appreciable amount of error. This is most likely due to error in exact material property values as they were all obtained from various sources in the literature and not directly measured. In particular, the electrolyte bulk modulus was hard to find a source for, so an order of magnitude sweep was performed for this value. This first resonance was seen to change the most. This indicates that further model calibration of certain material properties – in this case, the bulk modulus – can help hone in on sources of error in the model.

For the defective case, there is an observable downward shift in resonance location when compared with the pristine results. However, there is a significant error for all three resonances. This is also most likely attributed to errors in material properties, but the much larger error than with the pristine case implies that the error is more attributed to the defect case itself. In particular, this suggests that the embedded lithium defects may be thicker than 80 μm, as the experimental results show a larger shift in resonance location. X-Ray CT or laser metrology scans could be performed to confirm the inner structure and layer thicknesses of the batteries, and this information could then be used to properly inform the modeling. Overall, there is a good qualitative agreement between experimental and modeling results, which gives confidence in the model implementation. Further work as discussed, can be done to increase the quantitative results and eliminate sources of model error.

Chapter 4: Conclusion and Future Work

4.1 **Research Conclusions – Key Findings**

In this work, the local ultrasonic resonance spectroscopy (LURS) technique has been extended for immersion scans and contact transducer setups and is shown applicable for detecting defects in lithium metal batteries. The technique operates with a pulse-echo ultrasound setup and relies on a linear systems frequency-domain post-processing method to isolate the battery's reflection spectra from the measurement equipment.

The LURS technique was initially demonstrated for a single layer plate specimen case in which the through-thickness resonance frequencies appear as minima in the reflection spectra. These resonance frequencies are dependent on the plate's material properties and thickness. Slight angular offsets in the incident wave can cause significant shear mode conversion, which was seen

to influence LURS results on thicker plate specimens. These findings were corroborated by analytical modeling and 2D numerical modeling in COMSOL.

LURS feasibility was demonstrated for a functioning lithium metal battery. Significant shifts in resonance frequencies were observed with the introduction of embedded lithium chip defects. These shifts were significant in magnitude compared to the observed variance from repeat measurements. 2D plane strain COMSOL simulations of elastic and poroelastic wave propagation in full lithium metal battery systems agree qualitatively with these findings. Numerical error is still present in the results from these models due to uncertainty in material properties.

4.2 **Impact and Future Work**

This work has shown the proof-of-concept for a battery inspection method via the LURS technique. This technique is unique in that it isolates the specimen's local frequency response and is sensitive to battery defects, whereas previous techniques in the literature focused on SOC and SOH estimation via time-domain analysis. The presence of local lithium chip defects causes a downward shift in local resonance frequencies. Statistical analysis shows the low variance of the technique and multiphysics modeling agrees with the downward resonance shifts observed in the experimental measurements. Additional model calibration to better estimate the electrolyte and electrode material properties is expected to significantly improve the quantitative validation between experimental and simulated results.

So far, this work has assumed a constant SOC for the battery, so further experimental efforts can be made on tracking battery resonances through charge/discharge cycles. Furthermore, the embedded defects used in this work were coarse to test the efficacy of the technique, so testing more subtle defect conditions can help determine the sensitivity of the technique. Such defect cases could be with smaller embedded chips or lab-grown dendrites and lithium plating. This work

44

focused on single-point measurements, so extending this technique into full battery scans could give insight into resonance changes across the entire battery.

In addition, this work was done as a part of the NASA Convergent Aeronautics Solutions (CAS) project entitled Sensors based Prognostics to Avoid Runaway Reactions and Catastrophic Ignition (SPARRCI), which seeks to apply these types of inspection techniques to battery health monitoring with embedded sensors, machine learning, and prognostics tools. The multiphysics simulations have also laid the groundwork to support further inspection approaches of interest to the team, such as with bonded structural health monitoring (SHM) sensors or with guided wave approaches. This work will be continued through the end of 2022 by other NASA researchers working on the SPARRCI project.

References

[1] B. Liu, J. G. Zhang, and W. Xu, "Advancing Lithium Metal Batteries," *Joule*, vol. 2, no. 5, pp. 833–845, 2018, doi: 10.1016/j.joule.2018.03.008.

[2] C. Hendricks, N. Williard, S. Mathew, and M. Pecht, "A failure modes, mechanisms, and effects analysis (FMMEA) of lithium-ion batteries," *J. Power Sources*, vol. 297, pp. 113–120, 2015, doi: 10.1016/j.jpowsour.2015.07.100.

[3] P. Sun, R. Bisschop, H. Niu, and X. Huang, *A Review of Battery Fires in Electric Vehicles*, no. May. 2020.

[4] S. Sripad, A. Bills, and V. Viswanathan, "A review of safety considerations for batteries in aircraft with electric propulsion," *MRS Bull.*, vol. 46, no. 5, pp. 435–442, 2021, doi: 10.1557/s43577-021-00097-1.

[5] J. Darst, J. C. Thomas, D. P. Finegan, and E. Darcy, "Guidelines for Safe, High Performing Li-ion Battery Designs for Manned Vehicles," 2018.

[6] L. Cai and R. E. White, "Mathematical modeling of a lithium ion battery with thermal effects in COMSOL Inc. Multiphysics (MP) software," *J. Power Sources*, vol. 196, no. 14, pp. 5985–5989, 2011, doi: 10.1016/j.jpowsour.2011.03.017.

[7] H. Popp, M. Koller, M. Jahn, and A. Bergmann, "Mechanical methods for state determination of Lithium-Ion secondary batteries: A review," *J. Energy Storage*, vol. 32, no. September, p. 101859, 2020, doi: 10.1016/j.est.2020.101859.

[8] Z. Liu, Y. Qi, Y. X. Lin, L. Chen, P. Lu, and L. Q. Chen, "Interfacial Study on Solid Electrolyte Interphase at Li Metal Anode: Implication for Li Dendrite Growth," *J. Electrochem. Soc.*, vol. 163, no. 3, pp. A592–A598, 2016, doi: 10.1149/2.0151605jes.

[9] W. Waag, C. Fleischer, and D. U. Sauer, "Critical review of the methods for monitoring of

lithium-ion batteries in electric and hybrid vehicles," *J. Power Sources*, vol. 258, pp. 321–339, 2014, doi: 10.1016/j.jpowsour.2014.02.064.

[10] R. Bhattacharyya, B. Key, H. Chen, A. S. Best, A. F. Hollenkamp, and C. P. Grey, "In situ NMR observation of the formation of metallic lithium microstructures in lithium batteries," *Nat. Mater.*, vol. 9, no. 6, pp. 504–510, 2010, doi: 10.1038/nmat2764.

[11] S. A. Kayser, A. Mester, A. Mertens, P. Jakes, R. A. Eichel, and J. Granwehr, "Long-run: In operando NMR to investigate the evolution and degradation of battery cells," *Phys. Chem. Chem. Phys.*, vol. 20, no. 20, pp. 13765–13776, 2018, doi: 10.1039/c8cp01067f.

[12] Z. Wang, Z. Li, and Q. Liu, "Infrared thermography non-destructive evaluation of lithium-ion battery," *Int. Symp. Photoelectron. Detect. Imaging 2011 Adv. Infrared Imaging Appl.*, vol. 8193, no. September 2011, p. 81934I, 2011, doi: 10.1117/12.901592.

[13] J. B. Robinson *et al.*, "Detection of internal defects in lithium-ion batteries using lock-in thermography," *ECS Electrochem. Lett.*, vol. 4, no. 9, pp. A106–A109, 2015, doi: 10.1149/2.0071509eel.

[14] J. W. F. and D. A. S. A.G. Hsieh, S. Bhadra, B.J. Hertzberg, P.J. Gjeltema, A. Goy, "Environmental Science," *Energy Environ. Sci.*, 2012, doi: 10.4135/9781412975704.n47.

[15] P. Ladpli, F. Kopsaftopoulos, R. Nardari, and F.-K. Chang, "Battery charge and health state monitoring via ultrasonic guided-wave-based methods using built-in piezoelectric transducers," *Smart Mater. Nondestruct. Eval. Energy Syst. 2017*, vol. 10171, no. April 2017, p. 1017108, 2017, doi: 10.1117/12.2260107.

[16] P. Ladpli, F. Kopsaftopoulos, and F. K. Chang, "Battery state of charge estimation using guided waves - Numerical validation and statistical analysis," *Struct. Heal. Monit. 2017 Real-Time Mater. State Aware. Data-Driven Saf. Assur. - Proc. 11th Int. Work. Struct. Heal.*

Monit. IWSHM 2017, vol. 2, pp. 1839–1849, 2017, doi: 10.12783/shm2017/14066.

[17]   P. Ladpli, C. Liu, F. Kopsaftopoulos, and F. K. Chang, "Estimating lithium-ion battery state of charge and health with ultrasonic guided waves using an efficient matching pursuit technique," *9th Eur. Work. Struct. Heal. Monit. EWSHM 2018*, 2018.

[18]   P. Ladpli, F. Kopsaftopoulos, and F. K. Chang, "Estimating state of charge and health of lithium-ion batteries with guided waves using built-in piezoelectric sensors/actuators," *J. Power Sources*, vol. 384, no. October 2017, pp. 342–354, 2018, doi: 10.1016/j.jpowsour.2018.02.056.

[19]   L. Gold *et al.*, "Probing lithium-ion batteries' state-of-charge using ultrasonic transmission – Concept and laboratory testing," *J. Power Sources*, vol. 343, pp. 536–544, 2017, doi: 10.1016/j.jpowsour.2017.01.090.

[20]   C. Bommier *et al.*, "In Operando Acoustic Detection of Lithium Metal Plating in Commercial LiCoO2/Graphite Pouch Cells," *Cell Reports Phys. Sci.*, vol. 1, no. 4, p. 100035, 2020, doi: 10.1016/j.xcrp.2020.100035.

[21]   J. B. Robinson *et al.*, "Identifying Defects in Li-Ion Cells Using Ultrasound Acoustic Measurements," *J. Electrochem. Soc.*, vol. 167, no. 12, p. 120530, 2020, doi: 10.1149/1945-7111/abb174.

[22]   H. Li and Z. Zhou, "Numerical simulation and experimental study of fluid-solid coupling-based air-coupled ultrasonic detection of stomata defect of lithium-ion battery," *Sensors (Switzerland)*, vol. 19, no. 10, 2019, doi: 10.3390/s19102391.

[23]   NDT Resource Center, "Nondestructive Evaluation Techniques (Normal Beam Inspections)," *The Collaboration for NDT, Iowa State University*. https://www.nde-ed.org/NDETechniques/Ultrasonics/MeasurementTech/beaminspection.xhtml.

[24]   R. S. Dwyer-Joyce, B. W. Drinkwater, and C. J. Donohoe, "The measurement of lubricant-film thickness using ultrasound," *Proc. R. Soc. A Math. Phys. Eng. Sci.*, vol. 459, no. 2032, pp. 957–976, 2003, doi: 10.1098/rspa.2002.1018.

[25]   J. M. Allin, P. Cawley, and M. J. S. Lowe, "Adhesive disbond detection of automotive components using first mode ultrasonic resonance," *NDT E Int.*, vol. 36, no. 7, pp. 503–514, 2003, doi: 10.1016/S0963-8695(03)00045-8.

[26]   J. Maynard, "Resonant ultrasound spectroscopy," *Phys. Today*, vol. 49, no. 1, pp. 26–31, 1996, doi: 10.1063/1.881483.

[27]   J. Rus and C. U. Grosse, "Local Ultrasonic Resonance Spectroscopy: A Demonstration on Plate Inspection," *J. Nondestruct. Eval.*, vol. 39, no. 2, pp. 1–12, 2020, doi: 10.1007/s10921-020-00674-5.

[28]   L. Kinsler, *Fundamentals of Acoustics, 4th edition*. 2000.

[29]   Comsol, "Acoustic Reflections off a Water-Sediment Interface," pp. 1–32, 2013.

[30]   B. Parker, "Comparison of sound propagation in water-saturated sediment using different sediments in an Effective Density and Fluid model By Comparison of sound propagation in water-saturated sediment using 5 different sediments in an Effective Density and Fluid mode," no. February, 2006.

[31]   C. Hakoda, J. Rose, P. Shokouhi, and C. Lissenden, "Using Floquet periodicity to easily calculate dispersion curves and wave structures of homogeneous waveguides," *AIP Conf. Proc.*, vol. 1949, no. April, 2018, doi: 10.1063/1.5031513.

[32]   COMSOL Multiphysics, "Structural Mechanics Module," *Manual*, p. 454, 2018, [Online]. Available: www.comsol.de.

[33]   S. G. Johnson, "Notes on Perfectly Matched Layers (PMLs)," no. August 2007, pp. 1–18,

2021, [Online]. Available: http://arxiv.org/abs/2108.05348.

[34] M. Krumova, A. Flores, F. J. Baltá Calleja, and S. Fakirov, "Elastic properties of oriented polymers, blends and reinforced composites using the microindentation technique," *Colloid Polym. Sci.*, vol. 280, no. 7, pp. 591–598, 2002, doi: 10.1007/s00396-001-0646-z.

[35] B. Pal and M. Riyazuddin Haseebuddin, "Analytical Estimation of Elastic Properties of Polypropylene Fiber Matrix Composite by Finite Element Analysis," *Adv. Mater. Phys. Chem.*, vol. 02, no. 01, pp. 23–30, 2012, doi: 10.4236/ampc.2012.21004.

[36] D. P. Finegan *et al.*, "Characterising the structural properties of polymer separators for lithium-ion batteries in 3D using phase contrast X-ray microscopy," *J. Power Sources*, vol. 333, pp. 184–192, 2016, doi: 10.1016/j.jpowsour.2016.09.132.

[37] J. L. Jordan *et al.*, "Elastic properties of polyethylene from high pressure sound speed measurements," *Polymer (Guildf).*, vol. 212, no. July 2020, p. 123164, 2021, doi: 10.1016/j.polymer.2020.123164.

[38] A. Masias, N. Felten, R. Garcia-Mendez, J. Wolfenstine, and J. Sakamoto, "Elastic, plastic, and creep mechanical properties of lithium metal," *J. Mater. Sci.*, vol. 54, no. 3, pp. 2585–2600, 2019, doi: 10.1007/s10853-018-2971-3.

[39] E. J. Cheng, N. J. Taylor, J. Wolfenstine, and J. Sakamoto, "Elastic properties of lithium cobalt oxide (LiCoO 2)," *J. Asian Ceram. Soc.*, vol. 5, no. 2, pp. 113–117, 2017, doi: 10.1016/j.jascer.2017.03.001.

[40] C. Huang and P. S. Grant, "Coral-like directional porosity lithium ion battery cathodes by ice templating," *J. Mater. Chem. A*, vol. 6, no. 30, pp. 14689–14699, 2018, doi: 10.1039/c8ta05049j.

[41] F. Pouraghajan *et al.*, "Quantifying Tortuosity of Porous Li-Ion Battery Electrodes:

Comparing Polarization-Interrupt and Blocking-Electrolyte Methods," *J. Electrochem. Soc.*, vol. 165, no. 11, pp. A2644–A2653, 2018, doi: 10.1149/2.0611811jes.